Viscoelastic modelling of the tricuspid valve chordae tendineae tissue

Li-Wei Liu[a,*], Chung-Hao Lee[b], Ankush Aggarwal[c], Chih-Ming Chao[a], Colton J. Ross[b], Yu-Kai Liao[a]

[a] *Department of Engineering Science, National Cheng Kung University, Tainan 70101, Taiwan*
[b] *School of Aerospace and Mechanical Engineering, The University of Oklahoma, Norman, OK 73019, USA*
[c] *James Watt School of Engineering, University of Glasgow, United Kingdom*

Abstract

In the present study, the mechanical behavior of tricuspid valve (TV) chordae tendineae tissue is investigated experimentally and theoretically. A series of uniaxial mechanical testing experiments of the TV chordae tendineae is conducted and its viscoelastic model is developed by taking into account the initial condition of displacement of the tissue. Our experimental result shows the typical J-shaped force-displacement curve of the TV chordae tendineae and the corresponding viscoelastic model is established via a nonlinear spring is installed to replace the linear spring of the generalized Kelvin model. In addition, specified arrangements of the model parameters and the initial condition of the individual Kelvin element are proposed. The exact solutions of the model under step-wise and constant-rate forces are analytically derived and calibration of the model constants is addressed. The resulted simulation is compared with uniaxial mechanical testing of the TV chordae tendineae tissue and shows superior performance of the proposed model under creep and monotonic loading experiments. Furthermore, the sensitivity analysis and the parameter study of the model parameters are performed to examine the influence of initial conditions of displacement as well as other internal variables on the model response under step-wise and constant-rate forces.

Keywords: Chordae tendineae; viscoelastic model; the nonlinear generalized Kelvin model; creep response; uniaxial mechanical test.

1. Introduction

The chordae tendineae connect the papillary muscles to the mitral or tricuspid valve leaflets to prevent leaflet prolapse into the atria during systolic

*Corresponding author
Email address: liweiliu@mail.ncku.edu.tw (Li-Wei Liu)

closure, ensuring a unidirectional blood flow through the heart chambers over the cardiac cycle. *In vitro* characterizations of human, porcine, and ovine chordae tendineae revealed the typical J-shaped stress-strain responses [1, 2, 3], along with other intrinsic behaviors, such as an increased extensibility with an increased cross-sectional area, strain-rate dependency and an increased stiffness with age [4, 5, 6]. Other studies also showed that the myxomatous chordae exhibit disorganized collagen fibrils and lower failure stress compared to the the healthy counterparts [7, 8]. Regardless of the causal disease, the alteration in the mechanical properties and/or failure of the valvular chordae tendineae, such as in the case of rupture, elongation, thickening or retraction [9], can result in valve disorders like regurgitation [10].

To gain a deeper understanding of the cardiac mechanics and function, researchers constructed computational models of the mitral and tricuspid valve (TV) apparatus that is composed of the chordae structures. For example, linearly elastic spars were used to model the chordae tendineae in an asymmetrical model for the dynamic motion of the ovine mitral valve [11] and porcine tricuspid valve [12]. Alternative representations of the chordae tissue mechanics include the hyperelastic Ogden model to simulate the human mitral valve chordae in a patient-specific finite element framework [13], and an incompressible, isotropic hyperelastic form for an anatomically accurate mitral valve model [14]. To model tissue nonlinear mechanical behaviors, hyperelastic models were used to represent the *in vitro* characterization data for chordae tendineae tissues of human and animal mitral/tricuspid valves [15, 16].

Collectively, the research to date provides a thorough, fundamental understanding of the *hyperelastic* mechanics of the chordae; however, the viscous (*i.e.*, time-dependent) nature of the tissues has received sparse attention. The viscoelasticity of the chordae has been elucidated from uniaxial testing in the previous experimental works [6, 17, 18], and these behaviors have been demonstrated to be imperative for proper valve closing and function. For example, while it is hypothesized that healthy chordae exhibit minimal creep during the valve closing [19, 20], it is possible that in the case of *hypertension* the creep response drives the tissue remodeling and chordae elongation [21]. Further, the viscoelasticity of the chordae tissue is necessary to accurately model the strain-rate dependency, which has been shown in the previous experimental characterizations of the valve *leaflets* [22, 23, 24, 25] and is an important topic regarding *in-silico* modeling of valve function under elevated heart rates [26, 27]. Despite these experimental observations, the majority of the previous computational studies utilized a *linearly* or *non-linearly* elastic model to simulate the mechanics of the chordae tissue, without considering the essential viscous effects. Up to date, the viscoelastic model suitable for the chordae tissues has not been investigated, rendering an essential research topic for a more rigorous investigation of valvular chordae tissue biomechanics.

The formulation of a chordae-specific viscoelastic model requires an understanding of the classical viscoelastic theory. It is well-known that the Kelvin model has the infinite-valued instantaneous modulus and hence could not capture the fast-rate phenomena; the Maxwell model has the zero-valued asymp-

totic stress modulus and therefore is unsuitable for slow strain rates or creep; and the 3-parameter standard linear solid model has finite valued instantaneous and asymptotic moduli but possesses an inflexible type of relaxation/creep behavior [28, 29]. These facts were re-demonstrated for the application of the viscoelastic model to bio-mechanics [30]. While it is infeasible to develop a viscoelastic model addressing all the presented limitations, tissue-specific forms can be proposed that more accurately capture the physiologically relevant mechanics. In the case of the chordae tendineae viscoelasticity, creep properties and rate-dependency are the two key consideration, and thus, the generalized Kelvin model can serve as a foundation for developing and refining *in-silico* models. In this work, we aim to fill this gap in heart valve biomechanics knowledge by developing a chordae-specific viscoelastic model for the TV chordae tendineae tissue—utilizing a nonlinear generalized Kelvin (NGK) model in conjunction with holistic considerations of initial condition effects. The developed model will be validated using *in vitro* characterizations of porcine chordae tendineae, along with systematic evaluations of the model performance in capturing the nonlinear and viscoelastic responses of the chordae tissue

2. Methods and materials

2.1. Uniaxial mechanical testing of the tricuspid valve (TV) chordae tendineae

To evaluate the performance of the GK model and explore the influence of displacment initial condition, we used the TV chordae tendineae as an application tissue. In this section, the experimental procedures of uniaxial characterizations of the TV chordae tissue are described. Specifically, two types of mechanical testing were conducted, including (i) the creep tests, and (ii) the monotonic loading tests. The first creep mechanical testing type enabled us to check whether chordae is viscoelastic, or can be modeled by the traditional hyperelastic models. On the other hand, the monotonic loading testing type was used to observe whether the chordae behaves linearly or nonlinearly and whether this tissue involves rate-dependency or rate-independency.

2.1.1. Tissue preparation

Porcine hearts ($80 - 140\,\mathrm{kg}$, $1 - 1.5$ years of age, $n = 6$) were obtained from a local USDA-approved slaughterhouse (Country Home Meat Co., OK, USA), cleaned of blood clots, and kept in a freezer at $-20\,^{\circ}\mathrm{C}$ for prolonged storage. Within 1-2 days of tissue acquisition, hearts were thawed at room temperature in phosphate-buffered saline solution prior to chordae tissue preparation and mechanical testing. Then, the chordae tendineae were excised from the TV while preserving the papillary muscles and leaflet points of attachment based on our previous experimental protocol. We have shown that this mechanical testing protocol is comparable to other existing chordae testing schemes [16, 31, 32] (Fig. A.1a-b).

In this study, strut chordae of the tricuspid valve anterior leaflet (TVAL) were selected for mechanical testing because they have been previously shown

as the primary load-bearing components of the three anatomical classifications (*i.e.*, strut, basal, and marginal [33]) during the systolic closing of the TV. Chordae tissue specimens were then stored in phosphate-buffered saline solution in a refrigerated environment at 4 °C until later mechanical testing within 12 hours after dissection. Measurements of the chordae diameter D at three points about the center of the chordae were recorded with an Olympus CKX53 microscope at 10X magnification (Olympus America Inc., WA, USA) prior to the uniaxial mechanical testing. In the following, only the key experimental procedures will be described. Please refer to Appendix A for the details of the tissue preparation, experimental setup, and chordae mechanical testing.

2.1.2. Uniaxial mechanical characterizations of the TV chordae tissue

Following our prior studies [16, 32], uniaxial mechanical testing was performed using the BioTester mechanical testing system (CellScale Biomaterials Testing, Waterloo, Canada), equipped with 1.5 N load cells. Tissue samples were mounted by five-tined BioRakes, anchoring the papillary muscles and the TVAL to the BioTester system. A force-controlled uniaxial testing protocol was employed for characterizing the chordae tissue specimens (Fig. 1a). In brief, the TVAL chordae tissues were first subjected to *preconditioning*, which consists of six incremental steps (each with four loading/unloading cycles) to the targeted force $F = 0.2, 0.4, 0.6, 0.8, 1.0, 1.2\,\mathrm{N}$ at a rate of 4.42 N/min to restore the tissues to their *in-vivo* functional condition [34]. A maximum force of 1.2 N for the TVAL chordae tissues was chosen for its similarity to the force that the TVAL chordae experience under physiological loading, as observed in the previous *in-vitro* experiments [35, 36]. A loading rate of 4.42 N/min was used according to the equivalent loading rates from the previous chordae mechanical characterizations [16, 32]. After the preconditioning protocol, the tissue specimens were monotonically loaded to $F = 1.2\,\mathrm{N}$, followed by a 2-hr creep test during which the uniaxial force was kept constant and the tine-to-tine separation distance was continuously recorded. The chosen 2-hr duration of the creep test was adopted to be consistent with the previous valvular soft tissue characterization schemes (0.5-3 hr) [37, 38]. Throughout all the tests, the load cell force readings and tine separation distance were recorded at a frequency of 5 Hz.

Fig. 1b and Fig. 1c show the force-displacement history for the *monotonic* loading step and the creep displacement history response, respectively, clearly demonstrating the existence of the creep behavior. It is obvious that the GK model lacks the component to capture the nonlinear response of soft tissue, and that the traditional nonlinear (hyperelastic) model by itself cannot describe the viscous (time-dependent) characteristics of the chordae tissue. Thus, we proposed to use the nonlinear generalized Kelvin (NGK) model, in conjunction with the initial condition improvement, to model the mechanical responses of the TVAL chordae tissue as experimentally characterized. The next subsection will detail the theoretical formulations of this NGK model.

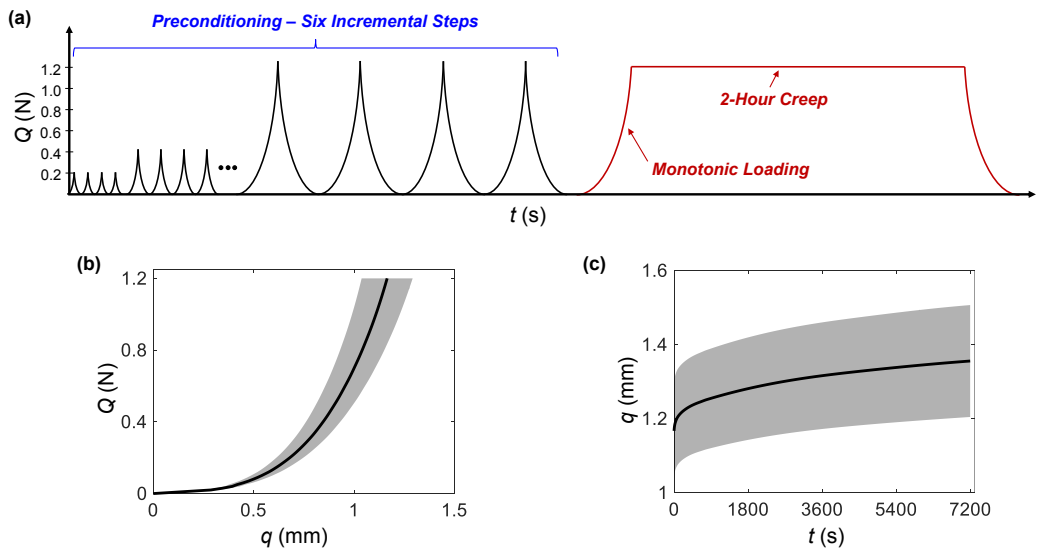

Figure 1: (a) Schematic of the uniaxial mechanical testing for characterizing TVAL chordae tendineae specimens ($n = 6$). (b) Force Q vs. displacement q response under the monotonic loading protocol, and (c) 2-hr creep response, displacement q versus time t—black solid lines denote the mean and the gray-shaded areas represent the standard error of mean.

2.2. Formulation of a nonlinear generalized Kelvin (NGK) model

Viscoelastic models are widely used to simulate the mechanical behavior of biological tissues. The well-known Maxwell and Kelvin models are often the first choice in the field of linear viscoelasticity. However, the limiting features of these two basic models, such as the infinite-valued instantaneous stiffness for the Kelvin model and the zero-valued asymptotic modulus for the Maxwell model, suggest that these two models might not be appropriate for simulating the mechanical behaviors of the tricuspid valve chordae. Therefore, in the present study, we chose the generalized models as our modeling candidates. Further, based on the experimental observations of our creep monotonic loading tests, the generalized Kelvin model[1] is selected for the development of viscoelastic model for the chordae tendineae.

2.2.1. Mathematical formulation of the NGK model

Now, we developed a model that consists of a nonlinear spring connected with M Kelvin element in series. This model is called the nonlinear generalized Kelvin (NGK) model hereafter and the mechanical element of our model is displayed in Fig. 2. Herein, q^{K_i}, Q^{K_i}, k_i, and c_i denote the displacement, the

[1]The detail of the generalized Kelvin model is reviewed in Appendix B.

force, the spring constant, and the damping coefficient associated with the i-th Kelvin element, respectively. For all our subsequent discussions, we call: (i) the displacement of the i-th Kelvin element $q^{\mathrm{K_i}}$, and (ii) the displacement of the nonlinear spring q^{S}, *the internal variables* of the NGK model.

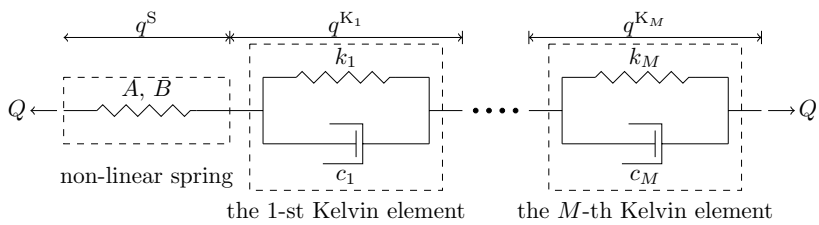

Figure 2: Schematic diagram of the nonlinear generalized Kelvin (NGK) model subject to a total force Q. The NGK model is organized by a nonlinear spring with spring constants A and B; spring displacement q^{S}; and a combination of M Kelvin elements: each consisting of a linear spring k_i and a linear dashpot c_i equipped with an internal state variable q^{K_i}.

The first component, which allows the representation of the chordae's J-shaped nonlinear mechanical behavior, is the replacement of the linear spring in the standard GK model (please see the details of the standard GK model in Appendix B) by a nonlinear spring. The constitution of this nonlinear spring is described by

$$Q^{\mathrm{S}} = f(q^{\mathrm{S}}), \tag{1}$$

where Q^{S} is the spring force as a nonlinear function f of q^{S}. In this work, we chose the following form that is motivated by the well-established Fung model in soft tissue biomechanics:

$$f(q^{\mathrm{S}}) = A\left[\exp\left(Bq^{\mathrm{S}}\right) - 1\right]. \tag{2}$$

Herein, A and B are the material parameters. On the other hand, the constitutive law of the i-th Kelvin elements can be formulated by [28, 29]

$$\dot{q}_i^{\mathrm{K}} = -\frac{k_i}{c_i} q_i^{\mathrm{K}} + \frac{1}{c_i} Q_i^{\mathrm{K}}, i = 1, 2, \cdots, M. \tag{3}$$

Since the nonlinear spring and the M Kelvin elements are connected in series, the total displacement q and the total force Q of our NGK model (Fig. 2) are computed by

$$Q = Q^{\mathrm{S}} = Q^{\mathrm{K}_1} = \cdots = Q^{\mathrm{K}_M}, \tag{4}$$

$$q = q^{\mathrm{S}} + \sum_{i=1}^{M} q^{\mathrm{K}_i}. \tag{5}$$

Specifically, the total force in the NGK model Q is equal to the force of every Kelvin element or the force of the outer-most nonlinear spring, and the total

displacement q is the sum of the displacements of both the nonlinear spring and all the Kelvin elements.

Then, the constitutive relations of the NGK model can be derived as follows:

$$\dot{q}^{\mathrm{K_i}} = -\frac{k_i}{c_i} q^{\mathrm{K}_i} + \frac{1}{c_i} Q, i = 1, 2, \cdots, M, \tag{6}$$

$$Q = f\left(q - \sum_{i=1}^{M} q^{\mathrm{K}_i}\right). \tag{7}$$

The subsequent discussion will be focused on the reduction in the number of model parameters to achieve tractable parameter estimation.

2.2.2. Geometric series to relate model parameters and initial conditions in the NKG model – Reduction in the number of model parameters

The second component of our developed NGK model for the chordae tendineae is the arrangement for the parameters that can significantly reduce the number of parameters in model calibration. We refer to the approach previously described in [39] that assumes the material constants in the Kelvin elements follow a geometric series:

$$\begin{aligned} k_i &= \alpha^{i-1} k_1, \\ c_i &= \beta^{i-1} c_1, \end{aligned} \quad i = 1, 2, 3, \cdots, M, \tag{8}$$

where k_1 and c_1 are the spring constant and the damping coefficient of the first Kelvin element, respectively, and α and β are the ratios of the spring constant and the damping coefficient between the i-th and $(i+1)$-th Kelvin elements, respectively.

By the similar token, we further arranged the initial condition of the Kelvin elements in a separate geometric series:

$$q^{\mathrm{K}_i}(t_0) = \gamma^{i-1} q^{\mathrm{K}_1}(t_0). \tag{9}$$

Herein, $q^{\mathrm{K}_1}(t_0)$ denotes the initial displacement of the first Kelvin element, and γ is the parameter linking the initial displacements between the i-th and the $(i+1)$-th Kelvin elements.

If both the initial force $Q(t_0)$ and the initial total displacement $q(t_0)$ are given, the initial displacement of the first Kelvin element can be determined

$$q^{\mathrm{K}_1}(t_0) = \frac{q(t_0) - f^{\mathrm{inv}}(Q(t_0))}{\sum_{i=1}^{M} \gamma^{i-1}}, \tag{10}$$

where

$$f^{\mathrm{inv}}(Q) := \left[\frac{1}{B} \ln\left(\frac{1}{A} Q + 1\right)\right]. \tag{11}$$

Therefore, the formulation of our NGK model becomes more concise, with the number of parameters reducing to 8 (*i.e.*, k_1, c_1, α, β, γ, A, B and M) compared to $2M+3$ (*i.e.*, $k_1, \cdots, k_M$, $c_1, \cdots, c_M$, A, B and M) in the case without the geometric series arrangements. With these two considerations being implemented, we can now analytically examine the model responses to different types of force input as will be discussed next.

2.2.3. Response of the NGK model to arbitrary forces

Let us consider the force-controlled testing commonly adopted in soft tissue characterizations. Our model formulation can be recast into the following form:

$$\dot{q}^{\mathrm{K}_i} = -\frac{\alpha^{i-1}k_1}{\beta^{i-1}c_1}q^{\mathrm{K}_i} + \frac{1}{\beta^{i-1}c_1}Q, \quad i = 1, 2, \cdots, M, \tag{12}$$

$$q = f^{\mathrm{inv}}(Q) + \sum_{i=1}^{M} q^{\mathrm{K}_i}, \tag{13}$$

where the analytical displacement solution of the i-th Kelvin element is

$$q^{\mathrm{K}_i}(t) = \exp[\frac{\alpha^{i-1}k_1}{\beta^{\mathrm{i}-1}c_1}(t_0 - t)]q^{\mathrm{K}_i}(t_0) + \frac{1}{c_i}\int_{t_0}^{t} \exp[\frac{\alpha^{i-1}k_1}{\beta^{\mathrm{i}-1}c_1}(\tau - t)]Qd\tau. \tag{14}$$

Note that the initial displacement $q^{\mathrm{K}_i}(t_0)$ is typically assumed to be zero in most of the biomechanics literature [40, 41, 42, 43] (*i.e.*, $q^{\mathrm{K}_i}(t_0) = 0$). However, a non-zero initial condition of the specimen is indeed present in the mechanical characterizations of biological materials, and the initial condition term in the closed-form solution in Eq. (14) does exist. For example, when the chorade tendineae tissue is under uniaxial characterizations, a *preconditioning* step is usually conducted prior to the uniaxial mechanical testing so that the tissue can be restored to a configuration that resembles its *in vivo* functional state.

This preconditioning step results in the deformation that should be treated as non-zero initial displacement condition (see Section 2.1.2 for details of the experiment testing procedure for chordae tendineae tissue). In the following, we seek to further explore the unique role of initial displacement condition in the mechanical behavior of our NGK model.

Derived analytically from Eqs. (13) and (14), we first demonstrated how the influence of initial conditions on the tangent compliance of the NGK mode:

$$C_t(t) = \frac{\dot{q}(t)}{\dot{Q}(t)} = \nabla f^{\mathrm{inv}}(Q) - \frac{1}{\dot{Q}}\sum_{i=1}^{M}\frac{\alpha^{i-1}k_1}{\beta^{i-1}c_1}q^{K_i} + \frac{Q}{\dot{Q}}\sum_{i=1}^{M}\frac{1}{\beta^{i-1}c_1}. \tag{15}$$

Clearly, if $f^{\mathrm{inv}} = 1/k_0$ and the geometric series for linking both model parameters in Eq. (8) and initial conditions in Eq. (9) are not employed, Eq. (15) reduces to Eq. (B.5) for the standard GK model (Appendix B).

2.2.4. Response of the NGK model to a stepped force

Now, let us consider the case that the NGK model undergoes a step-wise force input

$$Q(t) = \sum_{j=0}^{p} H(t - t_j)\Delta Q_j, \tag{16}$$

where ΔQ_i denotes the increment of force at time t_j, and $H(t - t_j)$ is the Heaviside function

$$H(t - t_j) = \begin{cases} 1 & t > t_j \\ 0 & t \leq t_j \end{cases}.$$

Based on the solution in Eq. (14), the displacement response of the NGK model to the step-wise force is

$$\begin{aligned} q(t) &= f^{\text{inv}}(\sum_{j=0}^{p} H(t - t_j)\Delta Q_j) \\ &+ \sum_{i=1}^{M} \left\{ \exp[\frac{\alpha^{i-1}k_1}{\beta^{i-1}c_1}(t_0 - t)]q^{\mathrm{K}_i}(t_0) + \sum_{j=0}^{p} \frac{1}{\alpha^{i-1}k_1} \left[1 - \exp(\frac{\alpha^{i-1}k_1}{\beta^{i-1}c_1}(t_j - t))\right] \Delta Q_j \right\}. \end{aligned}$$

This closed-form solution also demonstrates that the initial condition $q^{\mathrm{K}_i}(t_0) = \gamma^{i-1}q^{\mathrm{K}_1}(t_0)$ does affect the overall displacement response.

The creep test, which is a typical testing protocol to characterize biological tissues, is a special case of the mechanical testing experiments under a step-wise force where $Q(t) = H(t - t_0)\Delta Q_0$. Based on our analytical derivation, the displacement history of the NGK model subject to the creep test, considering non-zero $q^{\mathrm{K}_i}(t_0)$, is

$$\begin{aligned} \frac{q(t)}{\Delta Q_0} =: C(t - t_0) &= \frac{1}{\Delta Q_0} f^{\text{inv}}\left(H(t - t_0)\Delta Q_0\right) \\ &+ \sum_{i=1}^{M} \left\{ \exp[\frac{\alpha^{i-1}k_1}{\beta^{\mathrm{i}-1}c_1}(t_0 - t)]\frac{\gamma^{i-1}q^{\mathrm{K}_1}(t_0)}{\Delta Q_0} + \frac{1}{\alpha^{i-1}k_1}\left[1 - \exp(\frac{\alpha^{i-1}k_1}{\beta^{i-1}c_1}(t_0 - t))\right] \right\}. \end{aligned} \tag{17}$$

Further, we can derive the retardation time, t_C, for the proposed NGK model:

$$t_C = \frac{C(\infty) - C(0)}{\dot{C}(0)} = \frac{\frac{1}{\Delta Q_0} f^{\text{inv}}(\Delta Q_0) + \sum_{i=1}^{M}\left(\frac{1}{\alpha^{i-1}k_1} - \gamma^{i-1}q^{\mathrm{K}_1}(t_0)/\Delta Q_0\right)}{\sum_{i=1}^{M}\left(\frac{1}{\beta^{i-1}c_1} - \frac{\alpha^{i-1}\gamma^{i-1}k_1}{\beta^{i-1}c_1}\frac{q^{\mathrm{K}_1}(t_0)}{\Delta Q_0}\right)}. \tag{18}$$

In the above formulations, the initial condition clearly plays a role in both the creep response function and the retardation time of the NGK model.

2.2.5. Response of the NGK model to forces at a constant rate

In addition to the investigations of the NGK model response subjected to the step-wise force, the model response to forces at a constant rate is another case of interest. This scenario represents the behaviors as typically captured under monotonic loading experiments for the chordae tendineae tissue (see Section 2.1.2). Let us consider a force with a constant rate $Q(t) = R(t - t_0) + Q_0$ applied to the NGK model, where R is a constant. The solution in Eq. (13) brings us to the following displacement response

$$\begin{aligned} q(t) =& f^{\text{inv}}(R(t-t_0)+Q_0) + \sum_{i=1}^{M} \exp[\frac{\alpha^{i-1}k_1}{\beta^{i-1}c_1}(t_0-t)]\gamma^{i-1}q^{\text{K}_1}(t_0) \\ &+ \sum_{i=1}^{M} \frac{R}{\alpha^{i-1}k_1}\left\{t - t_0 \exp\left[\frac{\alpha^{i-1}k_1}{\beta^{i-1}c_1}(t_0-t)\right]\right\} \\ &+ \sum_{i=1}^{M}\left(\frac{Q_0 - Rt_0}{\alpha^{i-1}k_1} - \frac{R\beta^{i-1}c_1}{k_i^2}\right)\left\{1 - \exp\left[\frac{\alpha^{i-1}k_1}{\beta^{i-1}c_1}(t_0-t)\right]\right\}, \end{aligned} \tag{19}$$

and the tangent compliance

$$\begin{aligned} C_t(t) =& \frac{R}{B(R(t-t_0)+Q_0)+AB} + \sum_{i=1}^{M}\frac{1}{k_i} \\ &+ \left(\frac{Q_0}{R}\sum_{i=1}^{M}\frac{1}{c_i} - \sum_{i=1}^{M}\frac{1}{k_i} - \frac{1}{R}\sum_{i=1}^{M}\frac{k_i}{c_i}q^{K_i}(t_0)\right)\exp\left[\frac{k_i}{c_i}(t_0-t)\right]. \end{aligned} \tag{20}$$

Without loss of generality, an arbitrary force can be realized as a piece-wise linear input that resembles the experimental force measurements, *i.e.*,

$$Q(t) = R(t_{I+1} - t_I) + Q(t_I), t \in (t_I, t_{I+1}), \tag{21}$$

where t_I and t_{I+1} denote the I-th and the $(I+1)$-th time instants during testing.

With lengthy derivation (details not shown here), we arrive at the displacement response as follows:

$$q(t_{I+1}) = f^{\text{inv}}(R(t_{I+1}-t_I)+Q(t_I)) + \sum_{i=1}^{M}\gamma^{i-1}q^{\text{K}_1}(t_{I+1}), \tag{22}$$

$$\begin{aligned} q^{\text{K}_\text{i}}(t_{I+1}) =& \exp[\frac{\alpha^{i-1}k_1}{\beta^{i-1}c_1}(t_I - t_{I+1})]\gamma^{i-1}q^{\text{K}_1}(t_I) \\ &+ \frac{R}{\alpha^{i-1}k_1}\left\{t_{I+1} - t_I \exp\left[\frac{\alpha^{i-1}k_1}{\beta^{i-1}c_1}(t_I - t_{I+1})\right]\right\} \\ &+ \left(\frac{Q(t_I) - Rt_I}{\alpha^{i-1}k_1} - \frac{R\beta^{i-1}c_1}{\alpha^{2i-2}k_1^2}\right)\left\{1 - \exp\left[\frac{\alpha^{i-1}k_1}{\beta^{i-1}c_1}(t_I - t_{I+1})\right]\right\}. \end{aligned} \tag{23}$$

Therefore, the displacement response of the force-controlled tissue characterization experiments can be numerically determined based on the above equations.

2.2.6. Connection of the model parameters to overall tissue biomechanics

The tangent compliance of our developed NGK model serves as an indicator of the model predictivity of the displacement response for the chordae: Eq. (15) for arbitrary force and Eq. (20) for forces at a constant rate. On the other hand, the creep response function and the retardation time as analytically derived in Eqs. (17) and (18) show that the material constants A and B contribute to time (rate)-irrelevant responses.

In addition, the instantaneous modulus K_0, which is the capability of force response for the chordae under unit displacement input at the very beginning time t_0, is obtained as follows:

$$K_0 = BQ(t_0) + AB. \tag{24}$$

This exact formulation points out that the material constants A and B play the same role as the linear spring constant k_0 in the instantaneous modulus for the standard GK model.

2.3. Model parameter estimation and procedure for model fitting

To evaluate the performance of the proposed model as fitted to the acquired monotonic loading and creep testing data, the GK model with the geometric-series arrangement of the model parameters (named as the Kassab's model [44, 41] hereafter, see also Appendix) was compared with the NGK model and the following procedure was considered. After a preliminary analysis, the number of Kelvin elements M was first determined as the integer that resulted in the minimal functional value, and the rest of the viscoelastic and initial condition-related parameters (α, β, γ, k_1, and c_1) and elastic parameters (A and B for the NGK model or k_0 for the GK model) were determined by minimizing the difference between the model predictions and experimental measurements.

Specifically, creep and monotonic loading data from the two experimental protocols were used. From the creep test (Fig. 1c), the applied (constant) force and initial displacement were used as the model inputs, resulting in the predicted total displacement $q^{\mathrm{creep}}(t, \boldsymbol{c})$. Herein, $\boldsymbol{c}$ denotes a vector of all the model parameters (*i.e.*, elastic, initiation condition-related, and viscoelastic). Then, an intermediary non-parametric spline curve $\hat{q}^{(1)}(t)$ [45] was fit to the experimentally measured creep response history $\bar{q}^{(1)}(t_i)$. Note that the intermediary functions allowed us to smooth the experimental data and use samples at arbitrary time points. Similarly, under monotonic loading (Fig. 1b), an intermediary cubic polynomial function $\hat{Q}(t)$ was fit to the force $\bar{Q}(t_j)$, whereas the force $\hat{Q}(t)$ and initial displacement were used as an input to the model, resulting in the predicted total displacement $q^{\mathrm{mono}}(t, \boldsymbol{c})$. It was compared to the experimental displacement $\bar{q}^{(2)}(t_j)$ without the use of an intermediary function.

For minimizing the difference between the model predictions and the experimental measurements, the following functional with equal weights, *i.e.*, $w_1 = w_2 = 1.0$, assigned to both protocols was constructed:

$$\mathcal{F}(\boldsymbol{c}) = w_1 \int_{t_0}^{t_0+T} [q^{\text{creep}}(t, \boldsymbol{c}) - \hat{q}^{(1)}(t)]^2 dt + w_2 \sum_{j=0}^{N_d} [q^{\text{mono}}(t_j, \boldsymbol{c}) - \bar{q}^{(2)}(t_j)]^2, \quad (25)$$

where T is the time duration of the creep test and N_d is the total number of measurement points in the monotonic loading test. To numerically evaluate the integral, the time interval was divided into 20 equal segments, and a fifth-order Gauss quadrature rule was used in each segment. The inverse of parameters k_i and A were used in the minimization procedure in order to improve the conditioning, as recommended in [46, 47]. Rectangular bounds were used for the parameter values: $\alpha \in$(0.01, 100), $\beta \in$(0.01,500), $\gamma \in$(0.01,3000), $k_1 \in$(0.01,2500), $c_1 \in$(0.01,10000), $A \in$(0.01,50), $B \in$(0.01,100). The trust region reflective method [48] implemented in the SciPy package [49] was used in the minization procedure with arbitrary initial parameter guesses (*e.g.*, $\alpha = 3$, $\beta = 52$, $\gamma = 100$, $k_1 = 64.1\,\text{N/mm}$, $c_1 = 1146\,\text{N-s/mm}$, $A = 1\,\text{N}$, $B = 1\,\text{mm}^{-1}$ were used for the proposed NGK model).

3. Results

3.1. Fitting to creep testing data only

In the first demonstration, only the creep testing data is considered in model fitting (*i.e.*, $w_1 = 1.0$ and $w_2 = 0$). In general, the original Kassab's model does not accurately capture the experimentally-characterized 2-hour creep response (fitting error=0.0052-0.0478 mm-s), except for the TVAL-1 specimen (Fig. 3a). It is also noted that the Kassab's model prediction cannot fully represent the initial displacement of the creep response. These drawbacks are noticeably improved by introducing the initial condition improvement, Fig. 3b) for all the studied TVAL chordae specimens (fitting error=$0.0035 - 0.0085$ mm-s). Please see Appendix C for the formulation of the Kassab's model.

In addition, we also examined the performance of the GK model together with the initial condition improvement (Fig. 3c), and found that the decoupling between parameter k_0 (linear spring) and parameter k_1 (spring in the first Kelvin element) generally reduces the number of Kelvin elements while achieving a similar level of accuracy (fitting error=$0.0035 - 0.0124$ mm-s). Since the nonlinear spring (with parameters A and B) contribute to a constant creep response, we kept parameter B as unity when determining the model parameters of the proposed NGK model (Table 1). The NGK model predictions are in good agreement with the creep experimental data (fitting error=$0.0035-0.0161$ mm-s, the fitting results not shown).

3.2. Fitting to monotonic loading data only

According to the formulation of the displacement response in Eq. (B.9), we estimated the material constants of the GK model based on the experimental data of the chordae (see Section 3.2). Obviously, the agreement between

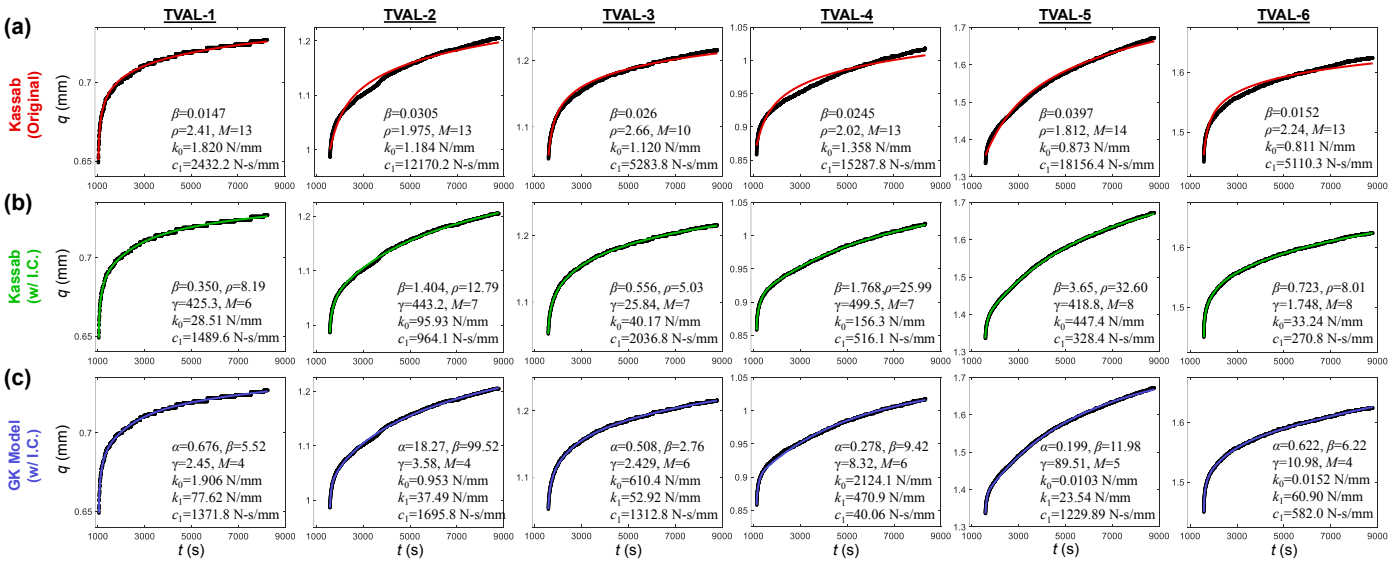

Figure 3: Comparisons of various model predictions with the creep data for the six TVAL chordae specimens: (a) the Kassab's model, (b) the Kassab's model with initial condition improvement, and (c) the GK model with initial condition improvement.

Table 1: Parameters of the proposed NGK model – fitting to the creep data only. In this study case, parameter B is set to $1.0\,\mathrm{mm}^{-1}$ and $A \in (0.01, 5000)$.

Specimen	α	β	γ	A (N)	k_1 (N/mm)	c_1 (N-s/mm)	M
TVAL-1	0.748	5.79	1010.6	1.300	83.17	1507.0	4
TVAL-2	0.345	13.52	2544.1	0.0107	23.20	1631.9	5
TVAL-3	0.363	4.23	7.04	1.450	56.98	1530.0	4
TVAL-4	0.223	9.06	11.25	4985.5	117.2	325.1	4
TVAL-5	0.225	7.01	59.08	0.0101	119.7	325.1	5
TVAL-6	0.458	22.73	2695.0	0.0356	24.47	1017.6	4

the simulation of the GK model and the experimental result is not able to be achieved, necessitating the required improvement of the standard GK model for modeling the chordae tissue.

To investigate the difference of model predictions between the GK and the NGK models, we performed the second demonstration by considering only the monotonic loading data in model parameter estimation ($w_1 = 0$, and $w_2 = 1.0$). As demonstrated in Figure 4, even though increasing the number of Kelvin elements could introduce a certain level of material's nonlinearity, the GK model, with the initial condition improvement, cannot represent the typical J-shaped force vs. displacement response of the TVAL chordae. In contrast, the proposed NGK model, which considers a nonlinear spring and initial condition improve-

ment, is able to accurately capture the nonlinear force-displacement behavior of all the six TVAL chordae specimens. The corresponding model parameters are summarized in Table 2. Note that very minimum viscous contribution is involved in the monotonic loading phase, so that the number of Kelvin elements is kept as constant ($M = 1$). This study case also demonstrates the necessity of introducing a nonlinear spring to the GK model to represent the nonlinear, viscous mechanical behaviors of biological tissues, such as the chordae tendineae of the tricuspid heart valve.

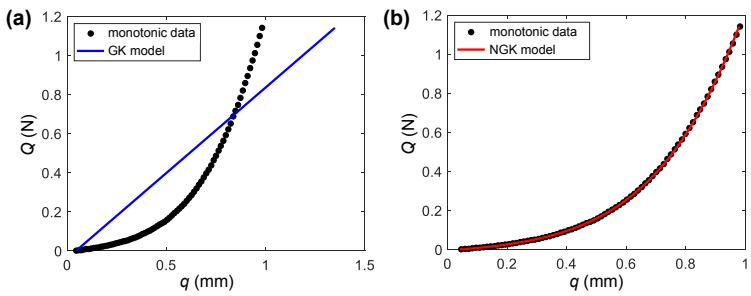

Figure 4: Comparison of the model predictions against the monotonic loading data of a representative specimen (TVAL-3) between: (a) the GK model, and (b) the NGK model.

Table 2: Parameters of the proposed NGK model – fitting to the monotonic loading data only. In this case, the number of Kevin elements M is set to be 1.

Specimen	α	β	γ	A (N)	B (mm^{-1})	k_1 (N/mm)	c_1 (N-s/mm)
TVAL-1	21.74	212.8	452.7	0.0367	6.53	0.0271	49.82
TVAL-2	17.54	305.3	1640.8	0.0550	4.02	0.557	42.33
TVAL-3	46.0	17.79	847.1	0.0250	4.31	0.0191	79.46
TVAL-4	15.58	373.6	2422.3	0.0279	5.03	13.95	8.81
TVAL-5	40.92	353.6	631.7	0.0471	3.12	0.0140	36.94
TVAL-6	39.87	441.3	247.5	0.0340	3.09	4.44	0.803

3.3. Fitting to both creep and monotonic loading data

In our final demonstration, both the monotonic loading and the creep testing data are considered in model parameter estimation ($w_1 = w_2 = 1.0$). As shown in Figure 5a-b and Table 3, the proposed NGK model can very accurately represent both the creep data and the monotonic loading data for all the six TAVL chordae specimens. This demonstrates the superior predictivity of the nonlinear, viscous mechanical behaviors of the studied biological tissues.

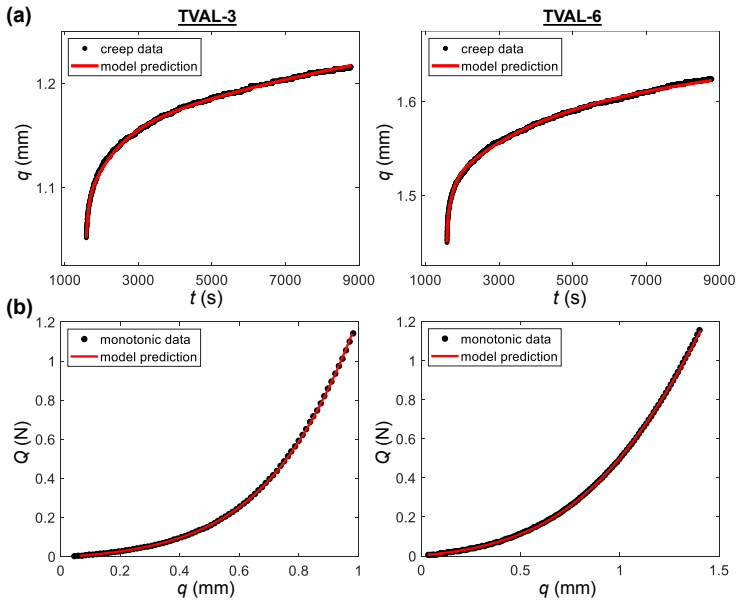

Figure 5: Representative results of the proposed NGK model fitting to both: (a) the creep data, and (b) the monotonic loading data – TVAL-3 and TVAL-6.

Table 3: Parameters of the proposed NGK model – fitting to both the creep and the monotonic loading data.

Specimen	α	β	γ	A (N)	B (mm)$^{-1}$	k_1 (N/mm)	c_1 (N-s/mm)	M
TVAL-1	0.682	14.41	1283.2	0.0353	6.81	51.52	1623.8	11
TVAL-2	0.341	6.87	1330.6	0.0543	4.19	88.64	501.5	10
TVAL-3	0.537	7.54	907.7	0.0245	4.39	34.97	1920.6	11
TVAL-4	0.409	4.71	282.0	0.0482	4.06	170.4	617.1	5
TVAL-5	0.192	12.33	53.85	0.0764	2.34	23.94	1178.4	6
TVAL-6	0.519	7.86	2.49	0.0272	3.29	54.72	564.0	12

3.4. Sensitivity analysis of the NGK model parameters

In addition to the above three demonstration cases, we also performed a sensitivity analysis to determine if the model parameters were well determined. Following the previously established methods [50], the eigenvectors and eigenvalues of the Hessian matrix $\mathbf{H}$ were determined and related to the ϵ-indifference (*i.e.*, error-indifference) region. Further, the determinant and the condition number of $\mathbf{H}$ were calculated, which can be related to the volume of the confidence region and the relative inter-specimen variability, respectively.

From the Hessian-based sensitivity analysis, we found that the model parameters were the well-determined for each specimen. First, the determinant of $\mathbf{H}$ was generally large (up to 1E30), indicating a small ϵ-indifference region (Table 4). Second, the condition number of $\mathbf{H}$ was relatively small, as compared

to the values reported in [50], suggesting a small variability of the given linear combination of parameters. Third, the magnitudes of the variances of the individual parameters were generally small (*i.e.*, 1E5 to 1E−9), with the exception of parameter γ, which was consistently associated with a higher variance up to 1E9. Overall, the parameter variances suggest α to be the best determined parameter, while γ is the least determined. Finally, from the eigenvector analyses, we found that the minimum eigenvalue was most commonly associated with α (*i.e.*, an eigenvector of $\sim\pm1$), while the maximum eigenvalue was generally correlated to γ (Table 5). These trends suggest that small changes in α will minimally affect the model predictions, whereas small changes in γ can have great effects on the model predictions. In summary, the NGK model parameters were well-determined with low sensitivity.

Table 4: Variance of the NGK model parameter for each specimen (see Table 3), which were determined as the diagonal component of $\mathbf{H}^{-1}$. The determinant det($\mathbf{H}$) and the condition number cond($\mathbf{H}$) are also reported.

Specimen ID	α	β	γ	A (N)	B (mm)$^{-1}$	k_1 (N/mm)	c_1 (N-s/mm)	det($\mathbf{H}$)	cond($\mathbf{H}$)
1	-6.50E-07	-3.25E-04	-3.83E+09	4.17E+00	-1.45E+05	-1.84E-03	-5.45E+00	1.41E-04	5.89E+15
2	-2.13E-08	-7.21E-06	6.71E+09	-2.85E-01	-5.17E+02	-1.78E-03	-9.47E-02	3.64E+04	3.14E+17
3	-1.21E-07	-1.85E-05	-1.38E+09	-2.68E-01	-2.63E+03	-3.24E-04	-1.89E+00	-7.86E+02	1.14E+16
4	-3.36E-08	-4.75E-06	2.95E+01	-5.48E-09	-1.15E-05	-1.01E-02	-2.34E-01	1.43E+27	5.39E+09
5	-8.86E-09	-2.23E-05	4.43E+02	-6.57E-04	-2.07E-01	-7.73E-05	-2.35E-01	4.63E+18	5.01E+10
6	-4.57E-08	-1.13E-05	1.61E-04	-1.68E-07	-6.33E-04	-5.04E-04	-1.21E-01	1.86E+30	2.65E+06

Table 5: The maximum and minimum eigenvalues of the NGK model parameter sets determined for each specimen (see Table 3), along with the associated eigenvectors.

Specimen	Eigenvalues		α	β	γ	A (N)	B (mm)$^{-1}$	k_1 (N/mm)	c_1 (N-s/mm)
1	Max	1.66E-01	1.10E-05	5.65E-04	2.05E-05	1.00E+00	1.17E-03	1.24E-03	5.83E-03
	Min	-1.54E+06	1.00E+00	-1.53E-07	-3.04E-10	-1.10E-05	-5.72E-08	-4.80E-08	-7.24E-10
2	Max	1.49E-10	-9.87E-11	-8.41E-09	-1.00E+00	-1.10E-08	-9.76E-06	-4.12E-08	-9.95E-08
	Min	-4.68E+07	1.00E+00	-2.72E-07	-9.84E-11	-2.41E-06	-3.12E-08	-6.09E-09	-1.45E-09
3	Max	0.00E+00	1.00E+00	-3.34E-07	-1.87E-10	-6.90E-06	-3.86E-08	-3.84E-08	-5.56E-10
	Min	-8.25E+06	1.00E+00	-3.34E-07	-1.87E-10	-6.90E-06	-3.86E-08	-3.84E-08	-5.56E-10
4	Max	3.39E-02	2.19E-10	2.84E-08	1.00E+00	1.64E-11	1.75E-08	3.77E-07	7.61E-07
	Min	-1.82E+08	9.88E-07	-2.83E-07	-1.64E-11	1.00E+00	-7.47E-08	-5.85E-10	-2.83E-10
5	Max	2.25E-03	4.80E-10	-2.05E-07	-1.00E+00	1.78E-08	-4.19E-07	-1.52E-07	-2.91E-06
	Min	-1.13E+08	1.00E+00	-6.14E-08	4.80E-10	3.38E-07	1.10E-08	-1.75E-09	-4.29E-10
6	Max	6.22E+03	-7.61E-08	-3.64E-06	-1.00E+00	7.48E-07	3.89E-07	-3.55E-06	-8.52E-09
	Min	-2.19E+07	1.00E+00	-3.05E-07	-7.61E-08	-1.10E-05	-6.59E-08	-1.88E-08	-1.84E-09

3.5. Parametric studies

3.5.1. Influence of initial conditions

Based on the formulation of the creep function of the NGK model, we can reach to unusual behavior in the case of $\gamma^{i-1}q^{\mathrm{K}_1}(t_0) > \Delta Q_0/(\alpha^{i-1}k_1)$. Specifically, Fig. 6 shows the displacement responses of the NGK model under a unit step force associated with five different values of initial displacement described in Table 6. This figure contains two realistic creep curves (IC-4 and IC-5) when

$\gamma^{i-1}q^{\mathrm{K}_1}(t_0) < \Delta Q_0/(\alpha^{i-1}k_1)$, two unusual, non-realist curves (IC-2 and IC-3) when $\gamma^{i-1}q^{\mathrm{K}_1}(t_0) > \Delta Q_0/(\alpha^{i-1}k_1)$, and one curve with no creep (IC-1) when $\gamma^{i-1}q^{\mathrm{K}_1}(t_0) = \Delta Q_0/(\alpha^{i-1}k_1)$. Note that the curves for $q^{\mathrm{K}_i}(t_0) > \Delta Q_0/k_i$ show the relaxation-type displacement response that is typically not observed experimentally in a creep test with a unit stepped force.

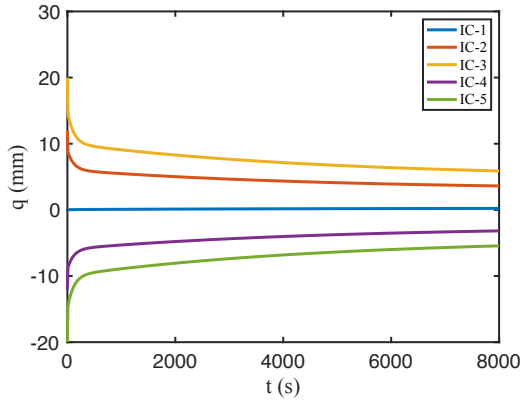

Figure 6: Response to the unit step force of the NGK model. (In the simulation, the material constants are $\alpha = 0.223$, $\beta = 9.06$, $\gamma = 11.25$, $A = 4985.5$ (N), $B = 1$ (mm)$^{-1}$, $k_1 = 117.2$ (N/mm), $c_1 = 325.1$ (N-s/mm), the element number is $M = 4$. The material constants used hereafter were estimated base on experiments of the TVAL chordae.)

Table 6: Initial condition for the response to the unit step force.

Initial condition	$q^{K_1}(t_0)$ (mm)	$q^{K_2}(t_0)$ (mm)	$q^{K_3}(t_0)$ (mm)	$q^{K_4}(t_0)$ (mm)
IC-1	0.0085	0.0034	0.0014	0.0005
IC-2	3.0085	3.0034	3.0014	3.0005
IC-3	5.0085	5.0034	5.0014	5.0005
IC-4	-2.9915	-2.9966	-2.9986	-2.9995
IC-5	-4.9915	-4.9966	-4.9986	-4.9995

In addition, considering another four different values of initial condition described in Table 7 as well as the zero-valued initial condition, we examined the overall tangent compliance (Fig. 7). The displacement response and corresponding tangent compliance were computed by five different values of initial conditions under monotonically increasing loading, demonstrating that the values of initial condition apparently affect both the overall displacement response (Fig. 7a) and the tangent compliance (Fig. 7b).

Further, the initial condition with a factor k_i/c_i controls the increase or decrease of the tangent compliance of the NGK model is shown in Fig. 8, where the five curves of tangent compliance correspond to five different values of initial condition summarized in Table 8.

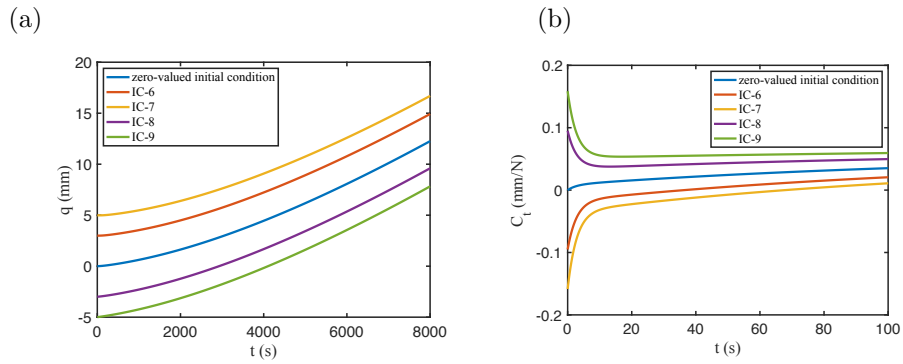

Figure 7: (a) Response and (b) tangent compliance of the NGK model. (In the simulation, the material constants are given as same values as shown in Fig. 6.)

Table 7: Initial conditions for the response to monotonically increasing force.

Initial condition	$q^{K_1}(t_0)$ (mm)	$q^{K_2}(t_0)$ (mm)	$q^{K_3}(t_0)$ (mm)	$q^{K_4}(t_0)$ (mm)
IC-6	0.0019	0.0216	0.2430	2.7335
IC-7	0.0032	0.0360	0.4050	4.5558
IC-8	-0.0019	-0.0216	-0.2430	-2.7335
IC-9	-0.0032	-0.0360	-0.4050	-4.5558

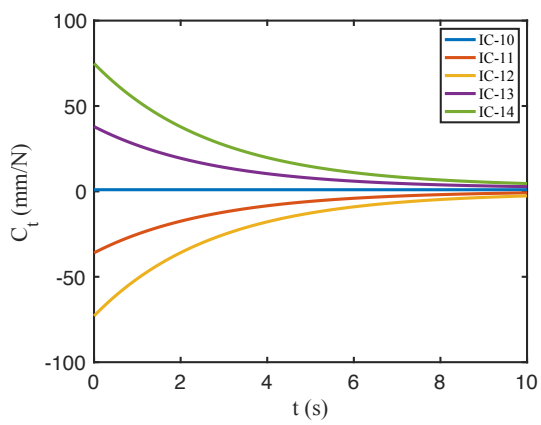

Figure 8: Tangent compliance of the NGK model in response to a force with a constant rate. (In the simulation, the material constants are given as same values as shown in Fig. 6.)

Note also that the initial condition $q^{\mathrm{K}_1}(t_0)$ of Kelvin elements does affect the retardation time t_C of the NGK model, as demonstrated in Fig. 9.

Table 8: Initial conditions of the NGK model in response to a force with a constant rate.

Initial condition	$q^{K_1}(t_0)$ (mm)	$q^{K_2}(t_0)$ (mm)	$q^{K_3}(t_0)$ (mm)	$q^{K_4}(t_0)$ (mm)
IC-10	-0.0002	-0.0431	-7.8559	-1431.3
IC-11	0.9998	0.9569	-6.8559	-1430.3
IC-12	1.9998	1.9569	-5.8559	-1429.3
IC-13	-1.0002	-1.0431	-8.8559	-1432.3
IC-14	-2.0002	-2.0431	-9.8559	-1433.3

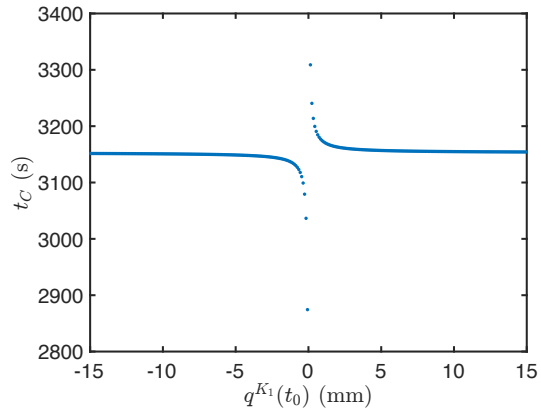

Figure 9: Retardation time with different $q^{\mathrm{K}_1}(t_0)$. (In the simulation, the materials constants are given as same values as shown in Fig. 6.)

3.5.2. Model response with non-zero-valued initial internal variables

Besides the investigation of different values of initial conditions, $q(t_0)$, as distributed to the Kelvin elements, we also consider the case of a zero-valued initial displacement $q(t_0) = 0$ in conjunction with non-zero-valued internal variables under the same monotonic loading: $q^{\mathrm{S}}(t_0)$ and $q^{\mathrm{K}_i}(t_0)$. Fig. 10 shows the displacement response and the tangent compliance of the NGK model (using the same material constants as shown in Fig. 6), associated with five different initial conditions of the four internal variables shown in Table 9. Interestingly, the results show that the non-zero-valued initial conditions of the internal variables have a clear influence on the response of the GK model even when the simulation begins with the same initial displacement.

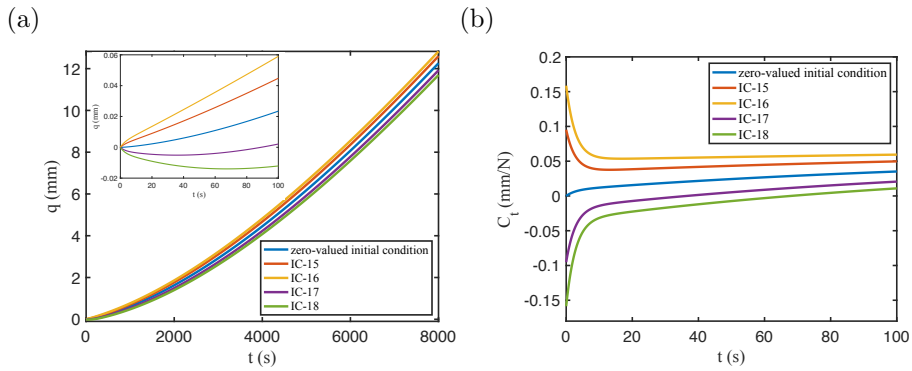

Figure 10: (a) Response and (b) tangent compliance of the NGK model for the zero-valued initial condition of displacement with non-zero-valued initial condition of the internal variables. (In the simulation, the material constants are the same values as shown in Fig. 6.)

Table 9: Non-zero-valued initial conditions of internal variables for the zero-valued initial condition of displacement.

Initial condition	$q^{K_1}(t_0)$ (mm)	$q^{K_2}(t_0)$ (mm)	$q^{K_3}(t_0)$ (mm)	$q^{K_4}(t_0)$ (mm)
IC-15	-0.0019	-0.0216	-0.2430	-2.7335
IC-16	-0.0032	-0.0360	-0.4050	-4.5558
IC-17	0.0019	0.0216	0.2430	2.7335
IC-18	0.0032	0.0360	0.4050	4.5558

3.5.3. Influence of material constants

The influence of the initial condition of the displacement and the internal variable have been investigated in the previous subsection. Herein, we also studied how the variations in the material constants affect the behaviors of the NGK model, including M, A, B, α, β, γ, k_1, and c_i.

The effect of different number of the Kelvin element, M is of investigation first. Consider the material constants estimated from the TVAL-3 specimen as shown in Table 3, we altered the value of M from 1 to 11 and simulate the response of NGK model under creep test. Figure 11 shows the response of the NGK model with different number of Kelvin elements. For $M = 1$, the NGK model behaves relaxation-type response whereas the model exhibit the common behavior in creep test when $M = 3$. Furthermore, the displacement of $M = 5$ and $M = 7$ are similar with the response of the NGK model with optimal values of parameters.

In addition, the effect of different values of M with the estimated parameter for the TVAL-4 specimen as shown in Table 1 was investigated. In this case, the displacement responses with of $M = 2$ and $M = 3$ exhibit relaxation behavior as shown in Fig. 11(c). The simulation also shows the larger value of M brings

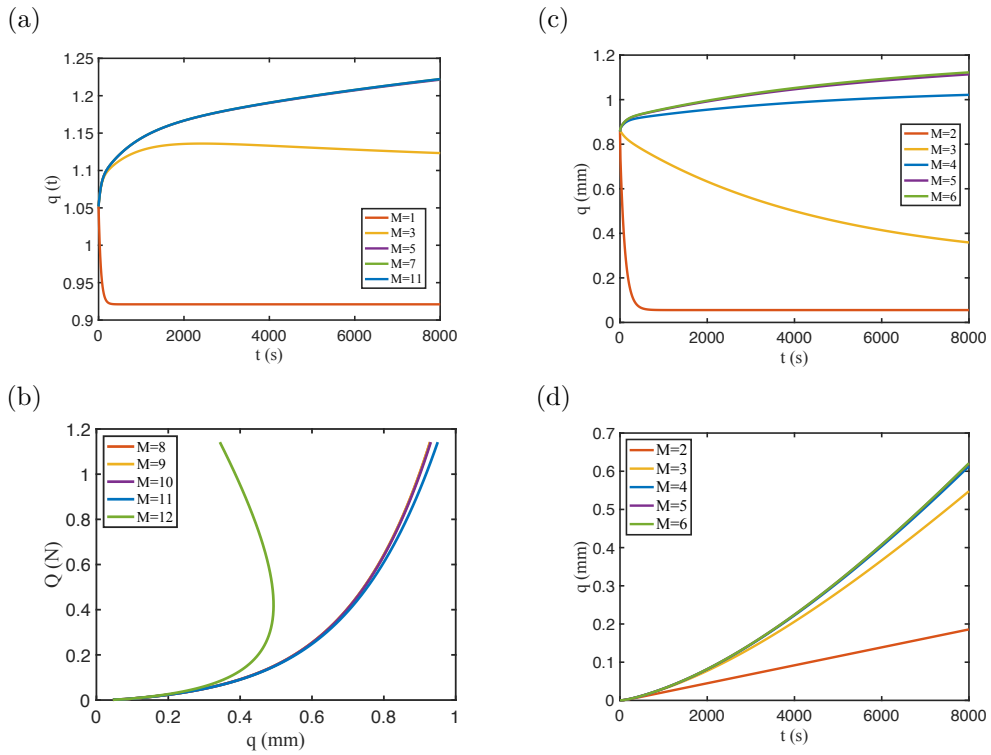

Figure 11: Responses of the NGK model under the creep and monotonic tests for different number of Kelvin elements. ((a) creep test and (b) monotonic test of TVAL-3, (c) creep test and (d) monotonic test of TVAL-4.)

larger value of displacement, however the displacement is slightly influenced when M is large then 4. Same influence of parameter M is observed in the monotonic loading test as shown in Fig. 11(d).

On the other hand, the influence of material constants α, β, k_1, and c_1 was examined and the result of displacement response under the creep test are shown in Fig. 12. These results indicate a larger displacement value with a smaller value of the material constant (α, β, k_1, or c_1). For the response under the monotonic loading, the results are shown in Fig. 13, which show the similar trend that the larger displacement is accompanied with a small value of α, β, k_1, or c_1.

Finally, we found that the influence of the parameter γ is almost negligible in the case of the initial condition $q(t_0) = 0$ for both creep and monotonic loading tests. However, if we applied the initial condition $q(t_0) = 1$ to the NGK model, the displacement response shows different behaviors associated with the different values of γ. In Fig. 14(a), the response of $\gamma = 2.25$ under creep displays a *relaxation-type* displacement, whereas the *creep-type* displacement was observed

when $\gamma \geq 5.625$. On the other hand, under monotonic loading Fig. 14(b) shows that the displacement response of $\gamma = 2.25$ and $\gamma = 5.625$ decreases firstly and then increases, together with three other scenarios possessing a monotonically increasing displacement response. All responses in both loading tests exhibit the larger value of γ the larger amount of displacement. It also echoes the sensitivity analysis in Section 3.4 that the small changes in γ can have great effects on the model predictions.

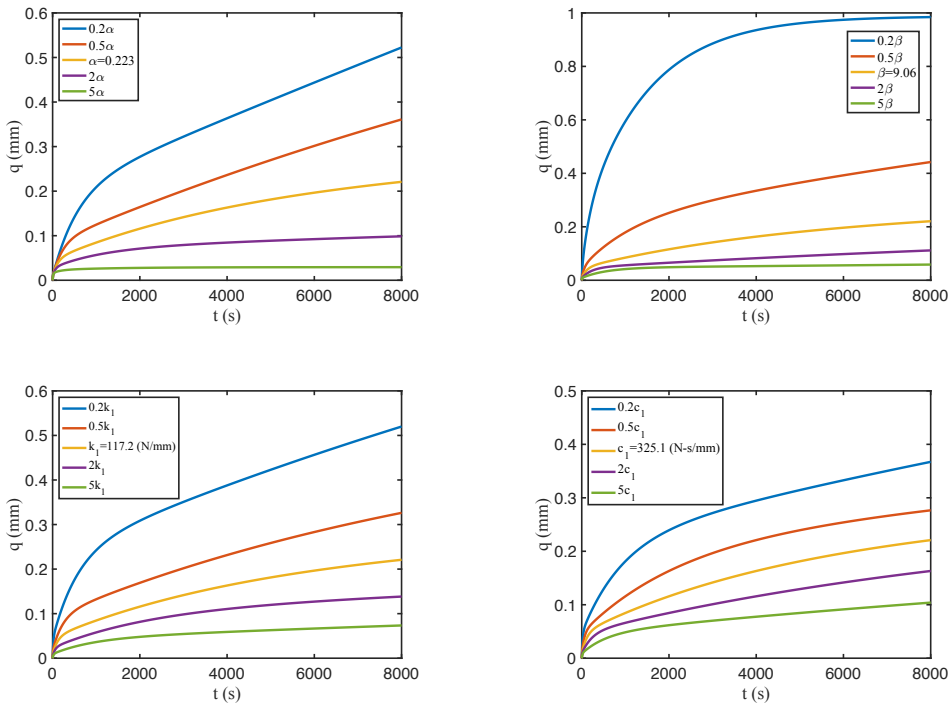

Figure 12: Responses of the NGK model under the creep tests for different values of parameter α, β, k_1, and c_1.

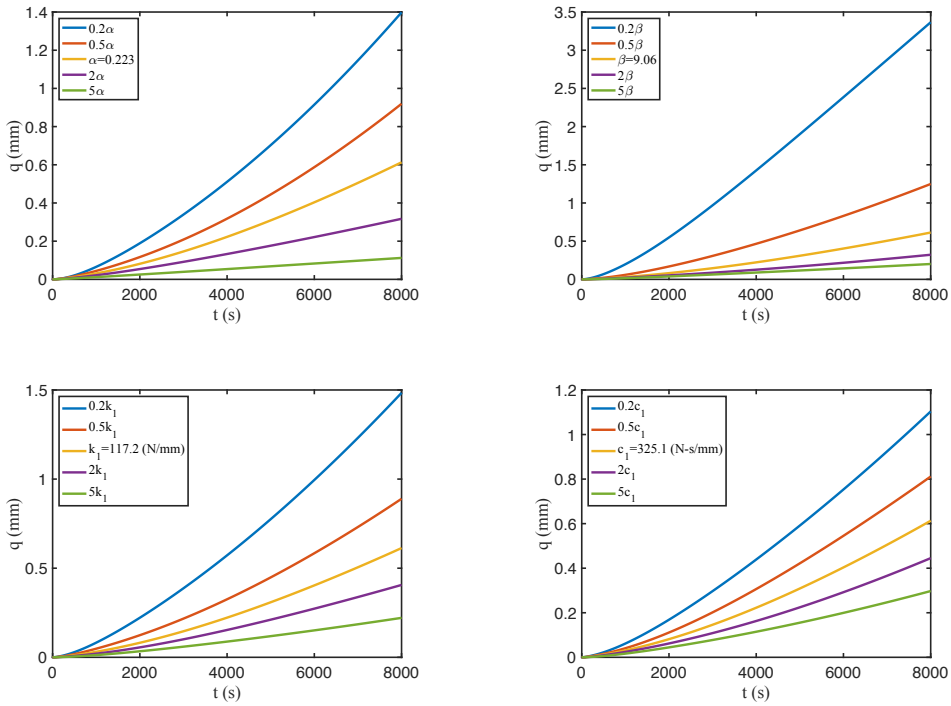

Figure 13: Responses of the NGK model under the monotonic loading test for different values of parameter α, β, k_1, and c_1.

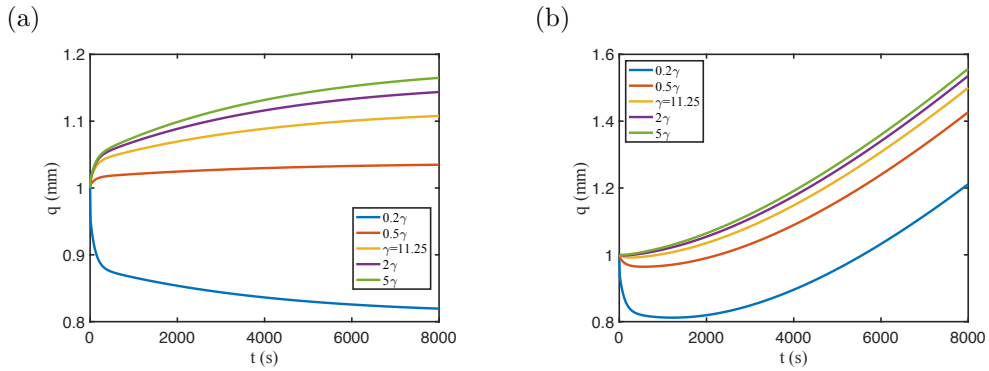

Figure 14: Responses of the NGK model under (a) the creep and (b) monotonic loading tests for different values of γ.

4. Discussions and conclusions

4.1. Overall findings and comparisons to the existing literature

In the present work, we have presented a unique viscoelastic model formulation specific to the tricuspid valve chordae tendineae that has been experimentally verified with *in vitro* tissue characterizations. The key advantages of our proposed NGK model are the relatively low number of model parameters, the low sensitivity (*i.e.*, well-determined parameters), the consideration of the initial displacement condition, and the capability to model the nonlinear stress-strain relationships. Altogether, the NGK model is robust for modeling both the creep and the monotonic loading conditions, both of which are physiologically relevant and can be incorporated to simulations of the heart valve closing.

To date, no studies have been performed to develop a viscoelastic model for the chordae tissues, limiting our comparisons to the existing literature. It is well-known that the GK model is well-suited for creep modeling as compared to the standard linear solid model or the Maxwell model. However, the GK model is limited as it can not accurately capture the J-shaped nonlinear mechanical behaviors of the chordae tendineae, which we have addressed in the developed NGK model. While some limitations of the model still exist, these may be addressed in future studies (see Section 4.2).

Experimentally, comparisons to the previous viscoelasticity-focused works for the chordae are limited. Primarily, the previous works focused on performing dynamic mechanical analysis to quantify the storage and loss moduli [18, 17], while another study focused on the stress relaxation properties [51] both of which are beyond the scope of the present study. In addition, this highlights another novel contribution of our work by quantifying the creep properties of the chordae. Meanwhile, with regards to the strain rate, we were able to similarly observe the tissue stiffening in response to a faster applied strain as was shown in a previous study [4].

4.2. Study limitations and future works

There are a couple limitations with the developed NGK model. First, the NGK model is one-dimensional and the area variation of the cross section of the chordae is neglected, hence the mechanical behavior on the plane of the cross section is not considered in this study. On the other hand, the sensitivity analysis revealed slightly worse-determined parameters for Specimen 1 and 2 as compared to the remaining specimens, as evident through a smaller determinant and larger condition of $\mathbf{H}$, and larger parameter variances. Nevertheless, the values were still within a reasonable range [50], and further refinements of the NGK model in future works or the experimental characterizations could yield more desirable sensitivity values.

From the experimental component of the present work there are a few limitations. For one, while it has been found that freezer storage has a negligible effect on the observed mechanics of the valve leaflets [52], it is possible that the papillary muscle mechanics could be affected. Another limitation is that by using

the leaflet-chordae-papillary muscle approach we can not directly quantify the contributions of the leaflet or papillary muscle segments to the viscoelastic characterizations; however, we previously found reasonable agreement between this testing scheme and other existing methods for isolated chordae (*i.e.*, no leaflet or papillary muscle segments) [31]. Finally, we used the machine crosshead displacements for our measurements, as opposed to the more accurate image-based digital image correlation techniques.

In future works, it will be worthwhile to investigate and implement the other considerations, such as the growth and remodeling or frequency behaviors, to complete the picture of the strengths and weaknesses of our developed NGK model. Additionally, while we have presented a comprehensive phenomenological viscoelastic model for the TV chordae tissues, the future development of a microstructure-based model could provide unique benefits. Similar to the models developed for tendons, cartilage, and skin [53, 54, 55], the fine-scale mechanical contributions of the collagen and elastin to chordae viscoelasticity could be better elucidated, which will be useful for diseased tissue modeling frameworks. Another useful scientific contribution could be realized by performing the model fitting to the creep and monotonic loading responses of diseased (*e.g.*, myxomatous) chordae to determine those parameters associated with a uniquely altered mechanical responses.

4.3. Concluding remarks

The experimental and theoretical study on mechanical behavior of TV chordae tendineae has been conducted in the present study. The uniaxial mechanical testing shows creep response and the typical J-shaped force-displacement curve of the TV chordae tendineae under stepped force and monotonic force loadings. The NGK model which consists of nonlinear spring in Eq. (2) and M Kelvin elements in series has been established for the TV chordae tendineae tissue by considering the non-zero initial condition of displacement for the chordae.

After the exact solution of displacement under stepped force and monotonic force with a constant rate have been obtained and the the calibration of model constants has been designed, the NGK model has been further validated by comparisons with experimental data under creep, monotonic loading, and force-rate varying loading conditions, demonstrating the acceptable accuracy of our proposed model. In addition, the exact solutions of the creep response function and the retardation time have also been derived. Comparing the NGK model to the classical viscoelastic theory, the NGK model demonstrated superior performance for the simulation under monotonic loading. Another benefit of our proposed NGK model is the computationally tractable number of 8 parameters compared to the classical GK requiring $2M + 1$ parameters.

Furthermore, sensitivity analysis of model parameters has be conducted, showing that the NGK model parameters were well-determined with low sensitivity. The effects and importance of the initial condition have been observed in the formulation of the exact solutions of the NGK model under step-wise and constant-rate force inputs as well as in the numerical demonstration. Fi-

nally, the parametric study has also been performed to illustrate the influence of material constants on the overall displacement prediction.

In summary, the NGK model has been developed and the superior model performance has been shown. Implementation of the NGK model in future heart valve simulations could be useful for capturing the rate-dependent behaviors, or the influences of creep on the diseased chordae behaviors, resulting in an improved simulation accuracy.

Appendix A. Chordae Tendineae Tissue Preparation and Testing

Porcine hearts were first dissected by removing the oracles and atria to reveal the TVs [31, 32]. Then, an incision was made from the septal-posterior leaflet commissure to the heart apex to open the ventricle, allowing for retrieval of the TV anterior leaflet (TVAL). The TVAL was carefully excised to ensure no damage was made to the chordae, leaflet, or papillary muscles, as shown in Figure A.1a. Then, the strut chordae were identified as the two thickest non-branched chordae on either side of the leaflet apex. Specimen preparation proceeded by trimming the excess tissue and muscle of the chordae-leaflet-papillary muscle entity such that the BioRake tines could easily pierce the papillary muscles without slippage, and there was no excess leaflet tissue (Fig. A.1b).

Chordae were then mounted to the BioTester via BioRakes (Fig. A.1c). After mounting, specimens were submerged in a phosphate-buffered saline bath heated to the physiological temperature (37 °C). Then, the linear actuators were jogged until the chordae were taut and the load cell force reading reached 10 mN. The uniaxial characterizations proceeded as: (i) preconditioning by cyclic repetitions of loading/unloading to the targeted force F, (ii) monotonic loading to the maximum target force, and (iii) 2-hour creep testing with a constant 1.2 N force.

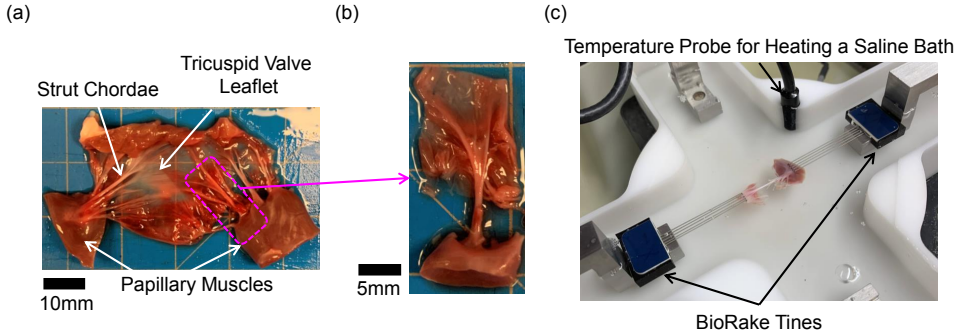

Figure A.1: (a) Experimental photo of a porcine tricuspid valve leaflet that was sectioned to the (b) leaflet-strut chordae-papillary muscle group for (c) uniaxial mechanical characterizations.

Appendix B. The generalized Kelvin model

The established generalized Kelvin (GK) model is our first candidate for modeling the uniaxial mechanical behavior of the chordae tendineae tissue. As illustrated in Fig. B.1, the GK model consists of one linear spring and M Kelvin elements arranged in series, with each Kelvin element representing the connection of a linear spring and a liner dashpot. In fact, the GK model covers a wide spectrum of viscoelastic models, including the standard linear solid model ($M = 1$). The theoretical study of the GK model is well-documented in the classical viscoleastic mechanics literature [56, 57, 28, 29, 58]. In the following, we brief review the constitutive relations of the GK model.

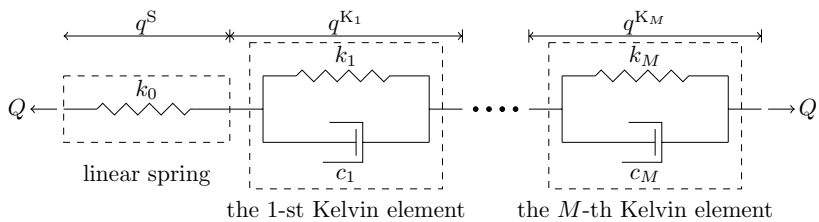

Figure B.1: Schematic of the generalized Kelvin (GK) model subject to a total force Q.

Firstly, the linear spring in Figure B.1 is governed by

$$Q^{\mathrm{S}} = k_0 q^{\mathrm{S}}. \tag{B.1}$$

where k_0 denotes the spring constant. On the other hand, the constitutive law of the i-th Kelvin elements is

$$\dot{q}_i^{\mathrm{K}} = -\frac{k_i}{c_i} q_i^{\mathrm{K}} + \frac{1}{c_i} Q_i^{\mathrm{K}}, i = 1, 2, \cdots, M. \tag{B.2}$$

Since the linear spring and the M Kelvin elements are connected in series, the total displacement q and the total force Q of the GK model in Fig. B.1 are formulated by

$$Q = Q^{\mathrm{S}} = Q^{\mathrm{K}_1} = \cdots = Q^{\mathrm{K}_M}, \tag{B.3}$$

$$q = q^{\mathrm{S}} + \sum_{i=1}^{M} q^{\mathrm{K}_i}. \tag{B.4}$$

Appendix B.1. Influence of initial displacement condition

Although the GK model is a well-known viscoelastic model, its capability of biomechanical simulation is not thoroughly explored in the literature of heart valve tissue mechanics. Therefore, in the following, we aim to address some of the issues of the application of the GK model that are related to the influence of initial condition.

The first demonstration is the influence of initial conditions on the tangent compliance of the GK model, which can be derived as follows:

$$C_t(t) := \frac{\dot{q}(t)}{\dot{Q}(t)} = \frac{1}{k_0} - \frac{1}{\dot{Q}(t)} \sum_{i=1}^{M} \frac{k_i}{c_i} q^{K_i}(t) + \frac{Q(t)}{\dot{Q}(t)} \sum_{i=1}^{M} \frac{1}{c_i}. \tag{B.5}$$

If we further consider a force with a constant rate $Q(t) = R(t - t_0) + Q_0$, where R is a constant, the tangent compliance becomes

$$\begin{aligned} C_t(t) = \frac{1}{k_0} + \sum_{i=1}^{M} \frac{1}{k_i} \\ + \left(\frac{Q_0}{R} \sum_{i=1}^{M} \frac{1}{c_i} - \sum_{i=1}^{M} \frac{1}{k_i} - \frac{1}{R} \sum_{i=1}^{M} \frac{k_i}{c_i} q^{K_i}(t_0) \right) \exp\left[\frac{k_i}{c_i}(t_0 - t) \right]. \end{aligned} \tag{B.6}$$

On the other hand, the displacement response to a step-wise force, $Q(t) = \sum_{j=0}^{p} H(t - t_j)\Delta Q_j$ is

$$q(t) = \frac{1}{k_0} \sum_{j=0}^{p} H(t - t_j)\Delta Q_j \tag{B.7}$$

$$+ \sum_{i=1}^{M} \left\{ \exp[\frac{k_i}{c_i}(t_0 - t)] q^{\mathrm{K}_i}(t_0) + \sum_{j=0}^{p} \frac{1}{k_i} \left[1 - \exp(\frac{k_i}{c_i}(t_j - t)) \right] \Delta Q_j \right\}. \tag{B.8}$$

Further, the response to a force with a constant rate $Q(t) = R(t - t_0) + Q_0$ is

$$\begin{aligned} q(t) = \frac{R(t - t_0) + Q_0}{k_0} + \sum_{i=1}^{M} \exp[\frac{k_i}{c_i}(t_0 - t)] q^{\mathrm{K}_i}(t_0) \\ + \sum_{i=1}^{M} \frac{R}{k_i} \left\{ t - t_0 \exp\left[\frac{k_i}{c_i}(t_0 - t) \right] \right\} \\ + \sum_{i=1}^{M} \left(\frac{Q_0 - Rt_0}{k_i} - \frac{Rc_i}{k_i^2} \right) \left\{ 1 - \exp\left[\frac{k_i}{c_i}(t_0 - t) \right] \right\}. \end{aligned} \tag{B.9}$$

All the above formulations under different kinds of forces detail the influence of the initial condition on the tangent compliance, as evidenced by the term associated with $q^{\mathrm{K}_i}(t_0)$.

Appendix B.2. Influence of initial conditions

The formulation in Eq. (B.7) enables us to formulate the creep function of the GK model ($q(t)/\Delta Q_0$ and $p = 0$) and also obtain unusual behavior in the

case of $q^{\mathrm{K_i}}(t_0) > \Delta Q_0/k_i$. Figure B.2 shows the displacement responses of the GK model under a unit step force associated with five different values of initial displacement including two realistic creep curves when $q^{\mathrm{K_i}}(t_0) < \Delta Q_0/k_i$ (IC-A2 and IC-A3), two unusual, non-realist curves when $q^{\mathrm{K_i}}(t_0) > \Delta Q_0/k_i$ (IC-A4 and IC-A5), and one curve with no creep when $q^{\mathrm{K_i}}(t_0) = \Delta Q_0/k_i$ (IC-A1).

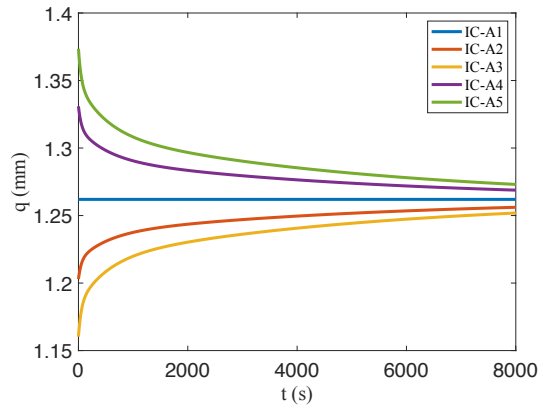

Figure B.2: Response to the unit step force of the GK model. In the simulation, the material constants are $k_0 = 1.0736$ (N/mm), $k_1 = 35.4597$ (N/mm), $k_2 = 25.8$ (N/mm), $k_3 = 18.7716$ (N/mm), $c_1 = 1784.71$ (N-s/mm), $c_2 = 13386$ (N-s/mm), $c_3 = 100390$ (N-s/mm), the element number is $M = 3$. The material constants used hereafter were estimated base on experiments of the chordae and the initial conditions are shown in Table B.1.

Table B.1: Initial conditions for the response to the unit step force.

Initial condition	$q^{K_1}(t_0)$ (mm)	$q^{K_2}(t_0)$ (mm)	$q^{K_3}(t_0)$ (mm)
IC-A1	0.0334	0.0459	0.0631
IC-A2	0.02	0.0275	0.0378
IC-A3	0.01	0.0137	0.0189
IC-A4	0.05	0.0687	0.0945
IC-A5	0.06	0.0825	0.1133

The tangent compliance with different values of initial condition, including the zero-valued initial condition, is shown in Fig. B.3. The displacement response and corresponding tangent compliance were computed by five different values of initial conditions under monotonically increasing loading, demonstrating that the values of initial condition obviously affect both the overall displacement response (Fig. B.3a) and the tangent compliance (Fig. B.3b).

Furthermore, the initial condition with a factor k_i/c_i controls the increase or decrease of the tangent compliance of the GK model as shown in Figure B.4, where the five curves of tangent compliance corresponding to five different values of initial condition.

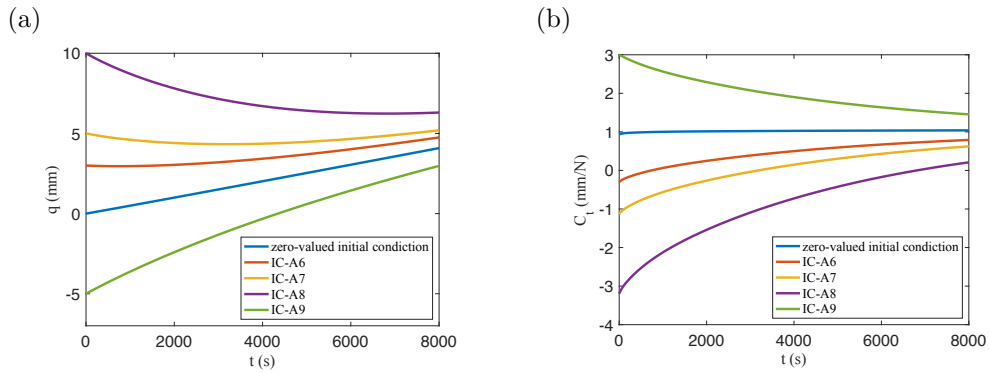

Figure B.3: Response and tangent compliance of the GK model. (In the simulation, the material constants are given as same values as shown in Fig. B.2 and the initial conditions are shown in Table B.2.)

Table B.2: Initial conditions for the response to the monotonically increasing force.

Initial condition	$q^{K_1}(t_0)$ (mm)	$q^{K_2}(t_0)$ (mm)	$q^{K_3}(t_0)$ (mm)
IC-A6	0.0003	0.0301	2.9696
IC-A7	0.0005	0.0502	4.9493
IC-A8	0.001	0.1005	9.8985
IC-A9	-0.0005	-0.0502	-4.9493

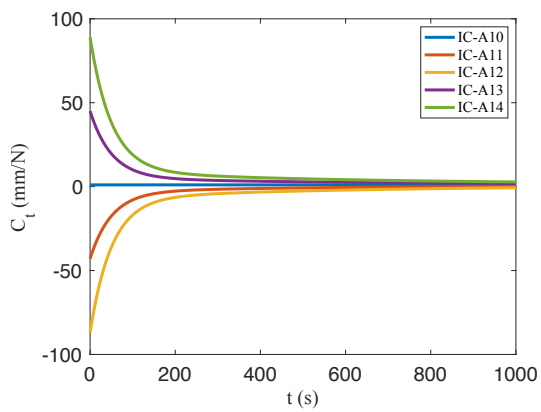

Figure B.4: Tangent compliance of the GK model in response to a force with a constant rate. (In the simulation, the material constants are given as same values as shown in Fig. B.3, the element number is $M = 3$ and the initial conditions are shown in Table B.3.)

Table B.3: Initial conditions for the response to a force with a constant rate

Initial condition	$q^{K_1}(t_0)$ (mm)	$q^{K_2}(t_0)$ (mm)	$q^{K_3}(t_0)$ (mm)
IC-A10	-0.0007	-0.0101	-0.1425
IC-A11	0.9993	0.9899	0.8575
IC-A12	1.9993	1.9899	1.8575
IC-A13	-1.0007	-1.0101	-1.1425
IC-A14	-2.0007	-2.0101	-2.1425

Appendix B.3. Model response with non-zero-valued initial internal variables

Besides the investigation of different values of initial conditions, $q(t_0)$, as distributed to the Kelvin elements, we also consider the case of a zero-valued initial displacement $q(t_0) = 0$ in conjunction with non-zero-valued internal variables under the same monotonic loading: $q^{\mathrm{S}}(t_0)$ and $q^{\mathrm{K}_i}(t_0)$. Figure B.5 shows the displacement response and the tangent compliance of the GK model (using the same material constants), associated with five different initial conditions of the two internal variables. Interestingly, the results show that the non-zero-valued initial conditions of the internal variables have a clear influence on the response of the GK model even when the simulation begins with the same initial displacement.

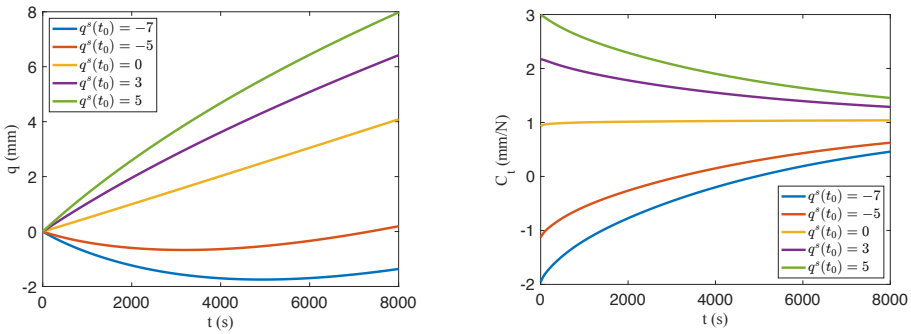

Figure B.5: Response of the GK model for the zero-valued initial condition of displacement with non-zero-valued initial condition of the internal variables. (In the simulation, the material constants are the same values as shown in Fig. B.3).

Appendix C. The Kassab's model – Generalized Kelvin Model with Geometric Series Assumptions

The creep response predicted by the GK model with M Kelvin elements is

$$q(t) = \frac{Q_0}{k_0} + \sum_{i=1}^{M} \frac{Q_0}{k_i} \left\{1 - \exp[-(t - t_0)/\tau_i]\right\}, \tag{C.1}$$

where t_0 and Q_0 are the initial time point and the applied (constant) force for the creep test, respectively, and $\tau_i = c_i/k_i$ is the retardation time of the i-th Kelvin element with its corresponding spring constant k_i and dashpot viscosity c_i. According to the earlier experiments by Kassab *et al.*, the following two geometric series were assumed that can represent the observed characteristic frequencies [41, 44].

$$\tau_i = \rho^{i-1}\tau, \text{ and } k_i = \frac{k_1}{(1+\beta)^{i-1}} \; i = 1, ..., M. \tag{C.2}$$

Herein, the spring of the first Kelvin element is related to the outmost linear spring by: $k_1 = k_0/\beta$. For an M series GK model, there are four parameter to be determined: k_0, c_1, β and, ρ.

Further incorporated with the initial condition improvement, the enriched Kassab's model ends up with five model parameters: k_0, c_1, β, ρ, and γ.

Acknowledgements

This research was supported by Ministry of Science and Technology of Taiwan (MOST 109-2221-E-006-004-MY3), the American Heart Association Scientist Development Grant (16SDG27760143), and the Presbyterian Health Foundation Team Science Grant. CJR was supported in part by the National Science Foundation Graduate Research Fellowship (GRF2020307284).

References

[1] R. E. Clark, Stress-strain characteristics of fresh and frozen human aortic and mitral leaflets and chordae tendineae: Implications for clinical use, The Journal of Thoracic and Cardiovascular Surgery 66 (1973) 202–208.

[2] K. S. Kunzelman, K. P. Cochran, Mechanical properties of basal and marginal mitral valve chordae tendineae, ASAIO Journal 36 (1990) M405–408.

[3] A. Pokutta-Paskaleva, F. Sulejmani, M. DelRocini, W. Sun, Comparative mechanical, morphological, and microstructural characterization of porcine mitral and tricuspid leaflets and chordae tendineae, Acta Biomaterialia 85 (2019) 241–252.

[4] K. O. Lim, D. R. Boughner, Mechanical properties of human mitral valve chordae tendineae: Variation with size and strain rate, Canadian Journal of Physiology and Pharmacology 53 (1975) 330–339.

[5] K. O. Lim, D. R. Boughner, Morphology and relationship to extensibility curves of human mitral valve chordae tendineae, Circulation Research 39 (1976) 580–585.

[6] K. O. Lim, D. R. Boughner, C. A. Smith, Dynamic elasticity of human mitral valve chordae tendineae, Canadian Journal of Physiology and Pharmacology 55 (1977) 413–418.

[7] K. O. Lim, D. R. Boughner, D. G. Perkins, Ultrastructure and mechanical properties of chordae tendineae from a myxomatous tricuspid valve, Japanese Heart Journal 24 (1983) 539–548.

[8] J. E. Barber, F. K. Kasper, N. B. Ratliff, D. M. Cosgrove, B. P. Griffin, I. Vesely, Mechanical properties of myxomatous mitral valves., Journal of Thoracic and Cardiovascular Surgery 122 (2001) 955–962.

[9] J. A. Casado, S. Diego, D. Ferreño, E. Ruiz, I. Carrascal, D. Méndez, J. M. Revuelta, A. Pontón, J. M. Icardo, F. Gutiérrez-Solana, Determination of the mechanical properties of normal and calcified human mitral chordae tendineae, Journal of the Mechanical Behavior of Biomedical Materials 13 (2012) 1–13.

[10] B. F. Waller, J. Howard, S. Fess, Pathology of mitral valve stenosis and pure mitral regurgitation-part II, Clinical cardiology 17 (1994) 395–402.

[11] K. H. Lim, J. H. Yeo, C. M. G. Duran, Three-dimensional asymmetrical modeling of the mitral valve: a finite element study with dynamic boundaries., Journal of Heart Valve Disease 14 (2005) 386–392.

[12] D. W. Laurence, E. L. Johnson, M.-C. Hsu, R. Baumwart, A. Mir, H. M. Burkhart, G. A. Holzapfel, Y. Wu, C.-H. Lee, A pilot in silico modeling-based study of the pathological effects on the biomechanical function of tricuspid valves, International Journal for Numerical Methods in Biomedical Engineering 36 (2020) e3346.

[13] Q. Wang, W. Sun, Finite element modeling of mitral valve dynamic deformation using patient-specific multi-slices computed tomography scans, Annals of Biomedical Engineering 41 (2013) 142–153.

[14] C.-H. Lee, J.-P. Rabbah, A. P. Yoganathan, R. C. Gorman, J. H. Gorman, M. S. Sacks, On the effects of leaflet microstructure and constitutive model on the closing behavior of the mitral valve, Biomechanics and Modeling in Mechanobiology 14 (2015) 1281–1302.

[15] K. Zuo, T. Pham, K. Li, C. Martin, Z. He, W. Sun, Characterization of biomechanical properties of aged human and ovine mitral valve chordae tendineae., Journal of the Mechanical Behavior of Biomedical Materials 62 (2016) 607–618.

[16] C. J. Ross, D. W. Laurence, M.-C. Hsu, R. Baumwart, Y. D. Zhao, A. Mir, H. M. Burkhart, G. A. Holzapfel, Y. Wu, C.-H. Lee, Mechanics of porcine heart valves'strut chordae tendineae investigated as a leaflet–chordae–papillary muscle entity, Annals of Biomedical Engineering 48 (2020) 1463–1474.

[17] M. Constable, H. E. Burton, B. M. Lawless, V. Gramigna, K. G. Buchan, D. M. Espino, Effect of glutaraldehyde based cross-linking on the viscoelasticity of mitral valve basal chordae tendineae, Biomedical Engineering 17 (2018) 93.

[18] A. G. Wilcox, K. G. Buchan, D. M. Espino, Frequency and diameter dependent viscoelastic properties of mitral valve chordae tendineae, Journal of the Mechanical Behavior of Biomedical Materials 30 (2014) 186–195.

[19] J. Ritchie, J. Jimenez, Z. He, M. S. Sacks, A. P. Yoganathan, The material properties of the native porcine mitral valve chordae tendineae: An in vitro investigation., Journal of Biomechanics 39 (2006) 1129–1135.

[20] S. Akhtar, K. M. Meek, V. James, Ultrastructure abnormalities in proteoglycans, collagen fibrils, and elastic fibers in normal and myxomatous mitral valve chordae tendineae, Cardiovascular Pathology 8 (1999) 191–201.

[21] W. H. McCullagh, J. W. Covell, J. Ross Jr, Left ventricular dilatation and diastolic compliance changes during chronic volume overloading, Circulation 45 (1972) 943–951.

[22] S. V. Jett, D. W. Laurence, R. P. Kunkel, A. R. Babu, K. E. Kramer, R. Baumwart, R. A. Towner, Y. Wu, C.-H. Lee, An investigation of the anisotropic mechanical properties and anatomical structure of porcine atrioventricular heart valves, Journal of the Mechanical Behavior of Biomedical Materials 87 (2018) 155–171.

[23] K. O. Lim, D. R. Boughner, Low frequency dynamic viscoelastic properties of human mitral valve tissue, Cardiovascular Research 10 (1976) 459–465.

[24] J. M. Lee, D. W. Courtman, D. R. Boughner, The glutaraldehyde-stabilized porcine aortic valve xenograft. i. tensile viscoelastic properties of the fresh leaflet material, Journal of Biomedical Materials Research 18 (1984) 61–77.

[25] A. H. Borghi, S. E. New, A. H. Chester, P. M. Taylor, M. H. Yacoub, Time-dependent mechanical properties of aortic valve cusps: Effect of glycosaminoglycan depletion, Acta Biomaterialia 9 (2012) 4645–4652.

[26] C. M. Otto, A. S. Pearlman, C. D. Kraft, C. Y. Miyake-Hull, I. G. Burwash, C. J. Gardner, Physiologic changes with maximal exercise in asymptomatic valvular aortic stenosis assessed by doppler echocardiography, Journal of the American College of Cardiology 20 (1992) 1160–1167.

[27] M. J. Thubrikar, J. L. Heckman, S. P. Nolan, High speed cine-radiographic study of aortic valve leaflet motion, J Heart Valve Dis 2 (1993) 653–61.

[28] R. S. Lakes, Viscoelastic solid, CRC Press, Boca Raton , Florida, USA, 1999.

[29] A. S. Wineman, K. R. Rajagopal, Mechanical Response of Polymers: an introduction, Cambridge University Press, New York, 2000.

[30] W. Zhang, A. Capilnasiu, D. Nordsletten, Comparative analysis of nonlinear viscoelastic models across common biomechanical experiments, Journal of Elasticity 145 (2021) 117–152.

[31] C. J. Ross, Z. Junnan, M. Liang, W. Yi, C. H. Lee, Mechanics and microstructure of the atrioventricular heart valve chordae tendineae: A review., Bioengineering (Basel) 7 (2020) 25.

[32] C. J. Ross, M.-C. Hsu, R. Baumwart, A. Mir, H. M. Burkhart, G. A. Holzapfel, Y. Wu, C.-H. Lee, Quantification of load-dependent changes in the collagen fiber architecture for the strut chordae tendineae-leaflet insertion of porcine atrioventricular heart valves, Biomechanics and Modeling in Mechanobiology 20 (2020) 223–241.

[33] M. D. Silver, J. H. C. Lam, N. Ranganathan, E. D. Wigle, Morphology of the human tricuspid valve, Circulation 43 (1971) 333–348.

[34] C.-J. Chuong, Y.-C. Fung, Residual stress in arteries, in: Frontiers in biomechanics, Springer, 1986, pp. 117–129.

[35] J. H. Jimenez, D. D. Soerensen, Z. He, S. He, A. P. Yoganathan, Effects of a saddle shaped annulus on mitral valve function and chordal force distribution: an in vitro study, Annals of Biomedical Engineering 31 (2003) 1171–1181.

[36] K. A. Khoiy, R. Amini, On the biaxial mechanical response of porcine tricuspid valve leaflets, Journal of Biomechical Engineering 138 (2016) 104504.

[37] J. A. Stella, J. Liao, M. S. Sacks, Time-dependent biaxial mechanical behavior of the aortic heart valve leaflet, Journal of Biomechanics 40 (2007) 3169–3177.

[38] C. E. Eckert, R. Fan, B. Mikulis, M. Barron, C. A. Carruthers, V. M. Friebe, N. R. Vyavahare, M. S. Sacks, On the biomechanical role of glycosaminoglycans in the aortic heart valve leaflet, Acta Biomaterialia 9 (2013) 4653–4660.

[39] W. Zhang, H. Y. Chen, G. S. Kassab, A rate-insensitive linear viscoelastic model for soft tissues, Biomaterials 28 (2007) 3579 – 3586.

[40] X. Ning, Q. Zhu, Y. Lanir, S. S. Margulies, A transversely isotropic viscoelastic constitutive equation for brainstem undergoing finite deformation, Journal of Biomechanical Engineering 128 (2006) 925–933.

[41] W. Zhang, X. Guo, G. S. Kassab, A generalized Maxwell model for creep behavior of artery opening angle, Journal of Biomechanical Engineering 130 (2008) 054502.

[42] R. Sopakayang, R. De Vita, A mathematical model for creep, relaxation and strain stiffening in parallel-fibered collagenous tissues, Medical Engineering & Physics 33 (2011) 1056–1063.

[43] S. K. Panda, M. L. Buist, A finite nonlinear hyper-viscoelastic model for soft biological tissues, Journal of Biomechanics 69 (2018) 121–128.

[44] W. Zhang, H. Y. Chen, G. S. Kassab, A rate-insensitive linear viscoelastic model for soft tissues, Biomaterials 28 (2007) 3579–3586.

[45] A. Aggarwal, A. M. Pouch, E. Lai, J. Lesicko, P. A. Yushkevich, J. H. Gorman III, R. C. Gorman, M. S. Sacks, In-vivo heterogeneous functional and residual strains in human aortic valve leaflets, Journal of Biomechanics 49 (2016) 2481–2490. Special Issue on Cardiovascular Biomechanics in Health and Disease.

[46] A. Aggarwal, An improved parameter estimation and comparison for soft tissue constitutive models containing an exponential function, Biomechanics and Modeling in Mechanobiology 16 (2017) 1309–1327.

[47] A. Aggarwal, Effect of residual and transformation choice on computational aspects of biomechanical parameter estimation of soft tissues, Bioengineering 6 (2019) 100.

[48] M. A. Branch, T. F. Coleman, Y. Li, A subspace, interior, and conjugate gradient method for large-scale bound-constrained minimization problems, SIAM Journal on Scientific Computing 21 (1999) 1–23.

[49] P. Virtanen, R. Gommers, T. E. Oliphant, M. Haberland, T. Reddy, D. Cournapeau, E. Burovski, P. Peterson, W. Weckesser, J. Bright, S. J. van der Walt, M. Brett, J. Wilson, K. J. Millman, N. Mayorov, A. R. J. Nelson, E. Jones, R. Kern, E. Larson, C. J. Carey, İ. Polat, Y. Feng, E. W. Moore, J. VanderPlas, D. Laxalde, J. Perktold, R. Cimrman, I. Henriksen, E. A. Quintero, C. R. Harris, A. M. Archibald, A. H. Ribeiro, F. Pedregosa, P. van Mulbregt, SciPy 1.0 Contributors, SciPy 1.0: Fundamental Algorithms for Scientific Computing in Python, Nature Methods 17 (2020) 261–272.

[50] J. R. Ligas, G. M. Saidel, F. P. Primiano Jr, Parameter estimation and sensitivity analysis of a nonlinearly elastic static lung model, Journal of Biomechanical Engineering 107 (1985) 315–320.

[51] J. Liao, I. Vesely, Relationship between collagen fibrils, glycosaminoglycans, and stress relaxation in mitral valve chordae tendineae, Annals of Biomedical Engineering 32 (2004) 977–983.

[52] G. A. Duginski, C. J. Ross, D. W. Laurence, C. H. Johns, C.-H. Lee, An investigation of the effect of freezing storage on the biaxial mechanical properties of excised porcine tricuspid valve anterior leaflets, Journal of the Mechanical Behavior of Biomedical Materials 101 (2020) 103438.

[53] P. Ciarletta, S. Micera, D. Accoto, P. Dario, A novel microstructural approach in tendon viscoelastic modelling at the fibrillar level, Journal of Biomechanics 39 (2006) 2034–2042.

[54] T. Osawa, T. Matsumoto, H. Naito, M. Tanaka, Evaluation of viscoelastic property of articular cartilage based on mechanical model considering tissue microstructure, Journal of Biomechanical Science and Engineering 7 (2012) 31–42.

[55] O. Lokshin, Y. Lanir, Viscoelasticity and preconditioning of rat skin under uniaxial stretch: Microstructural constitutive characterization, Journal of Biomechanical Engineering 131 (2009).

[56] W. Flu ugge, Viscoelasticity, Springer, Heidelberg, 1975.

[57] R. M. Christensen, Theory of Viscoelasticity, Academic Press, New York, 1982.

[58] D. Gutierrez-Lemini, Engineering Viscoelasticity, Springer US, New York, 2013.